Supplementary material for Neininger et al., 2021, Comparing airborne TD emission estimates for methane against BU emission inventories for the Surat Basin, Australia,
Phil. Trans. R. Soc. A. doi: 10.1098/rsta.2020.0458

Comparing airborne TD emission estimates for methane against BU emission inventories for the Surat Basin, Australia

Content:

Glossary

altitude elevation height	These three terms are not used randomly. Whenever possible, the following principle applies: An altitude of a flight track or a CBL top is above sea level [mAMSL], whereas the height of a flight or a CBL top is above the surface [mAGL], and 'elevation' is used for the topography of the terrain.
BU	Bottom-Up emission estimate using emission factors for known sources defining an emission inventory on an annual basis (*tons per year)*, down-scaled to *kilograms per hour* for the comparisons with our TD emission estimates. See also *'UNSW inventory*'.
CBL	Convective Boundary Layer (see section I)
CH_4	Methane
column mass	The mass of (excess) CH_4 in a vertical column (see section E)
concentration	Concentrations are always used as molar fractions, i.e. ppm or ppb
CSG	Coal Seam Gas
GFS	Global Forecast System *https://www.ncdc.noaa.gov/data-access/model-data/model-datasets/global-forcast-system-gfs*
mAGL	Height in metres above ground level
mAMSL	Altitude (flight) or elevation (terrain) above mean sea level
MoDiM	Monte Carlo Diffusion Model
slice	A connection between an upwind pixel and a downwind pixel along a backwards trajectory (figure 2 in the main article, and explanations in section E). In contrast to a trajectory, a slice is three-dimensional, i.e. it has a width, a length and a vertical extent defining a volume over an elongated area
SRTM	Shuttle Radar Topography Mission *https://www2.jpl.nasa.gov/srtm/*
TD	Top-Down emission estimate derived from airborne measurements. Due to the emissions' episodic character, the units used are *kilograms per hour* rather than *tons per year* as in the BU emission inventory
transect	A transect is a part of a flight that was used for the calculation of mass balances. Usually these transects were flown along straight lines on heights between 150 and 300 m above ground. A transect can consist of several flight legs on different altitudes. See also 'wall'.
UNSW	The University of New South Wales (UNSW Sydney)
UNSW inventory	Emission inventory compiled by Bryce Kelly's research group (*https://www.science.unsw.edu.au/our-people/bryce-kelly*). This inventory contains 4615 CSG wells, 395 other point-sources and 6056 distributed sources and is valid for 2018.
wall	A 'wall' of air along a transect is a volume of air between the surface and the top of the CBL containing the 'column masses' along the transect

Supplementary material for Neininger et al., 2021, Comparing airborne TD emission estimates for methane against BU emission inventories for the Surat Basin, Australia,
Phil. Trans. R. Soc. A. doi: 10.1098/rsta.2020.0458

A Details about the UNSW emission inventories

A general discussion about the UNSW CH_4 emission inventory is presented in the main article, where the figures SF1 to SF3, and the tables ST1 to ST3 are referenced. Comprehensive details on the quantities and emission factors for each CH_4 source category are provide in tables ST1 and ST2.

B Details about the flight tracks and their planning

The pre-existing knowledge about the methane sources in the Surat Basin spatially limited the measurements to two main clusters with diameters of about 50 km (see the yellow polygons in figures SF5 through SF13). These two clusters combined fill a rectangle of about 50 km by 150 km along the basin. Flight patterns were designed with the aim to quantify the emissions within the full rectangle as well as from sub-regions within. This included 'Lagrangian patterns', i.e., to follow the moving air mass along the wind between a background transect at the beginning, and one or up to four consecutive downwind transects thereafter. This strategy is shown schematically in figure SF16.

Even when the air masses under the actual conditions were well mixed within the Convective Boundary Layer (CBL, see section I), some vertical information was necessary. This was achieved by flying on two heights above the ground within the CBL, and vertical soundings up to above the CBL before the first transect, and after the last one. In most cases, additional soundings were flown between the transects. It was especially important to gain sufficient information about the top of the growing CBL.

Due to a technical problem with one of the two fully equipped aircraft we had to adapt plans to a scenario, where flight tracks of about 700 km length per day were sufficient to fly the transects and soundings as described above. The consequence was to fly fewer transects per day, and to fly twice per day on four of the seven days. When the average wind was along the basin (figures SF9, SF12 and SF13), the transects had to be at least 50 km long in order to capture the emissions of a whole cluster, or even longer than 150 km on the two days where both clusters were mapped during crosswind situations (figures SF10 and SF11). The time for the transects was limited by the development of the CBL, i.e. not earlier than when the CBL reached about 1000 mAGL, and not later as about the daytime temperature maximum on the surface, because afterwards, the vertical mixing is suppressed and the top of the actual CBL cannot be quantified anymore. Generally, this time-window was between 11 and 16 LT, with a tolerance for the ferry flights into the region and back.

As in any weather-dependent field work, compromises had to be made. During the first two days, the individual clusters were surveyed at about 150 m above the ground using a raster pattern to characterise the spatial structure of the CH_4 concentrations from the multiple CH_4 source categories. For this purpose, the transects were already aligned perpendicular to the wind, however not yet with a Lagrangian spacing in between (figures SF7 and SF8). On the last day – having already captured two complete along-the-basin-patterns and two cross-the-basin-patterns, some individual sources were visited. However, the emphasis in this article is on the six days that were suitable to derive regional and sub-regional balances.

For the planning of the Lagrangian patterns we used the 24-hour wind field forecast from the global GFS model to develop trajectories. Those trajectories were used to define the Lagrangian transects in the moving-map display in the cockpit. On this map that also showed air space information, the flight tracks were adapted in a way that restricted air space e.g. around military air bases was avoided. Two examples of planning-trajectories are shown in figure SF14.

Such a draft pattern for a day could have been adapted during the flight when the onboard wind measurements would have strongly deviated from the forecast. However, this was never the case. Even turning winds were forecasted sufficiently well for a good planning. This was not only an impression during the field-phase but was confirmed when analysing the data. Of course, the wind at different heights is not constant (wind shear), and hence the air is not moving as a rigid block. However, when taking the average wind on the height, where most flights took place between 150 and 300 mAGL, the wind shear during these convective conditions was not larger than the lateral diffusion of the emissions. Even when some vertical shear was distorting plumes, they were captured on the downwind transects. More details are discussed in the section N about using a dispersion model for assessing non-ideal conditions.

Already during the planning of the campaign, we knew, that a source attribution will be difficult for two reasons: (i) many co-located mixed sources; (ii) measuring ethane was not an option (see main article). Therefore, it was very fortunate that the six main observation days covered different wind regimes. This offered a chance, that a source attribution can also be made via geographical and statistical reasoning, using the information from the isotopes in the bag samples as discussed in section C.

C Collection of the airborne bag samples

During the airborne campaign 90 air samples were collected by pumping air into 3 litre SKC FlexFoil PLUS sample bags with polypropylene fittings. The bags were filled manually in the cockpit via a PU tubing, feeding ambient air from the intake and a Viton membrane pump in the right-hand underwing pod. Each bag took approximately one to two minutes to fill (recorded for each bag), and great caution was applied not to capture possibly contaminated air from the cockpit, i.e. flushing the fitting before opening the valve. The positions where the bag samples were taken are shown in figures SF9 to SF13. For instance, bags were filled at the plume cross sections shown in figures SF17 and SF24. The air samples from all days were analysed for $d^{13}C\_CH_4$, and samples on the 15th and 16th Sep 2018 were also analysed for dD_CH_4. Preliminary results are presented in [SR1] and the presentation that accompanies that abstract. Comprehensive details on the methods of measurement are discussed in [SR2]. These samples will be analysed in a future paper (Lu et al. in preparation).

D The overall approach (workflow)

Figure SF15 is showing the workflow from the measurements to the emission estimates. The focus in this publication is on the top-down emission estimates (TD) for 32 sub-regions and their comparison with existing bottom-up emission inventories (BU). In the following, some of these steps are explained in more detail, and the last steps (last two boxes in SF15) will allow a discussion and an outlook in sections L to O.

E Details about the mass balance method

An overview on different principles for a mass balance is summarised in the main article.

A correct mass balance depends on accurate column masses, i.e. the conversion from measured concentrations along the transects has to consider the air density (hence temperature and humidity) and the extent of the vertical mixing, i.e. at least a correct altitude of the top of the convectively mixed boundary layer (CBL). For these very low concentration differences between up- and downwind transects in the order of 10 ppb CH_4 it is also important to confirm that any instrumental drift or artefacts in the background concentrations can be excluded, or at least limited. Finally, the wind field must be known as well as possible. All these aspects are addressed in this supplement, after introducing the basic concept of our mass balances in this section.

The column mass as introduced in figure 2 of the main article as the total mass of methane within the observed Convective Boundary Layer, expressed in kg CH_4 per km^2. This primary use of 'column mass' is independent from its vertical distribution (the shape of the concentration profile), and it can be expressed as a total mass, or as the mass exceeding the 'background', i.e. subtracting the mass of methane that was already present in the observed mass of air when it arrived upwind of the region. At this stage we are assuming that we can convert the concentration measurements along the transects to 'excessive column masses', considering the background concentrations and the growth of the CBL.

Figure 2 of the main article illustrates how the column masses can be used for estimating the emissions from the areas between transects. For each pixel on the downwind transect the algorithm determines from which pixel on the upwind transect the air was originating. The backwards trajectories are calculated based on the measured wind (details see section K). Naturally, this pairing of upwind- and downwind-pixels is only approximate. Yet when averaging over the area, this has no effect. Since we do not know exactly from which pixel the air is coming, the column masses on the upwind transects are smoothed with a 5-km-moving average. This smoothing reduces the scattering of the individual results for slices as shown in figure 2 in the main article or in figure SF6 but has no relevant influence on the averaged result for the whole area between the two transects. Some secondary effects are discussed in connection with error estimates in section N. Furthermore, the smoothing allows extending the upwind transect by a few kilometres with the argument that – since the precise origin of the air is unknown – one can accept some approximation by an average column mass at the edges on the upwind side. This is observable in figure SF9, where bal_15_4 is accepting backwards trajectories that are outside of the third transect.

Each coloured pixel on the insert in figure 2 of the main article with the dimension d^2 (1 km^2 in this case) is characterising a column mass as kg CH_4 above each pixel. With a horizontal inflow (flux of CH_4) plus the emission flux balancing the outflow, this can be written as:

$$v_1 \cdot m_1/d^2 + e/d = v_2 \cdot m_2/d^2 \qquad \text{(eq. 1)}$$

where v_1 and v_2 are the wind components along the y-axis[1] (positive from upwind to downwind), m_1 and m_2 are the column masses connected via a trajectory defining a slice. The unit is mass per length and time [$kg \cdot s^{-1} \cdot m^{-1}$], or more practically [$kg \cdot h^{-1} \cdot km^{-1}$], i.e. kg CH_4 that are transported per hour through each 1 km wide slice into or out of the area between the two walls. e is the emission rate [kg/hr] within this whole slice.

v1 ≠ v2 would indicate divergence or convergence in the wind field. This is possible on a small scale, for instance when observing an individual plume from a chimney, but it is not acceptable on the given scale in this study because it would lead to a high dependency of the result on the local wind field. Small differences in the measured wind speeds that are varying in time would lead to completely different results, because the relative differences $(m_2 – m_1)/(m_2 + m_1)$ are small. We therefore need to assume a divergence free flow (no loss or gain of air mass in the horizontal). This does not mean that there is no exchange of CH_4 mass by lateral turbulent diffusion, or by divergence above the CBL.

If $v_1 = v_2 = v$ we can write v as $v = s/t$ (eq. 2)

where s is the north-south distance of the pixels, and t is the travel time of the air mass.

(eq. 1) can then be written as

$$(s/t) \cdot m_1/d^2 + e/d = (s/t) \cdot m_2/d^2 \qquad \text{(eq. 3)}$$

Multiplication by d and re-arrangement leads to

$$e = a \cdot (m_2 - m_1) /(t \cdot d^2) = n \cdot (m_2 - m_1)/t, \text{ or } e/a = (m_2 - m_1) /(t \cdot d^2) \qquad \text{(eq. 4)}$$

with $a = s \cdot d$, i.e. the area of the slice, and $a = n \cdot d^2$.

Equation (eq. 4) is the mathematical description for figure 2 in the main article: The gain of column mass divided by the travel time and multiplied by the number of steps of length d between the two walls is equal to the emission rate in this slice.

In other words, the column of air on d^2 (1 km^2 in this case) is picking up mass while traveling from the upwind wall to the downwind wall. The average column masses at the pixels in between are growing at the same rate as this column experiences when passing along the trajectory. It is important to realise that uncertainty in the modelled wind fields lead to uncertainty in the spatial attribution of sources to slices, i.e., into which pixels/columns along the slices ground-based sources are emitting. Therefore, instead of expressing specific emission rates for slices we better define accumulated or averaged emissions for several slices up to the size of the sub-region, or for a newly split smaller sub-region. The second version of eq. 4 is expressing the emissions per area along a slice. The integration to a larger area can be made by using either of the two. Note that here we report only emission estimates at sub-regional level, but the method may be used as well for individual or multiple slices.

The calculation of column masses along the transects is straight forward if we can assume that the vertical mixing between the surface and the top of the CBL is perfect, we know the mixing height (including the relevant topography of the surface as discussed in section I, and we know the 'background concentration' as discussed in section J.

[1] In this study, all wind fields had a dominating northerly or southerly component. If this is not the case, a coordinate transformation can align the y-axis with the average wind direction.

With these idealised assumptions, the mass m of CH_4 within a vertical column consisting of voxels 'i' of air with the dimensions of (x,y,z) 1 km x 1 km x dz_i is

$$m = \Sigma dz_i \cdot M \cdot \rho_M \cdot c_i; \qquad \text{(eq. 5)}$$

where dz_i is the depth of the layers (50 m except near the surface), M is the molar mass of CH_4 (16.042 kg/kmol), ρ_M is the molar density (kmol/m^3) of the atmosphere in each voxel, and c_i is the concentration (dry molar fraction of CH_4) above the background concentration [ppb].

<u>In the main article, this (eq. 4) is (eq. 1) and this (eq. 5) is (eq. 2).</u>

For the column mass, m is integrated between the first voxel over the surface (where dz and hence the volume is adjusted according to the elevation of the surface in this pixel) until the last voxel within the CBL. This scheme would – in principle – allow other vertical concentration profiles than constant. The vertical profile of the molar density 'ρ_M' is from interpolated averaged profiles, i.e. all the measurements of a day – especially from the vertical soundings – are averaged to the same layers of 50 m thickness with a temporal spacing of half an hour. Missing temperatures below the measured ones are extrapolated with 10 K/km (dry adiabatic), and those above the CBL are not relevant.

F Electronic supplements

In https://drive.switch.ch/index.php/s/3LFUn0d7OhU7s2R, three sets of graphical and numerical data are available:

- All mass balances in 32 sub-regions: Each of the 32 sub-regions is defined by the up- and downwind transects, and the range for the slices. This concept is explained with figure SF6, and all the sub-regions are sketched in figures SF7 to SF12. Another illustration is figure 2 in the main article. Here, the complete collection of kmz files for the sub-regions and their colour-coded slices are provided.
- Overview plots for all the flights with maps and vertical profiles as described in section H and figure SF18.
- Airborne data with a temporal resolution of 1 Hz and a description.

G Details about the combination of overlapping sub-regions

The 32 sub-regions for which we calculated emission estimates (figure 4 in the main article and table ST4) can be combined to a total emission estimate (figure 5 in the main article, and table ST6). However, this is not trivial because these 32 sub-regions are overlapping in a complex way. The sum of the emissions from the 32 overlapping sub-regions is certainly not the total for the region. Averaging emission rates per area in overlapping sub-regions per pixel is not an option as well, because from the pure mass balance as described above, the location of the emissions within the sub-regions are unknown and hence cannot be combined easily when the sub-regions are not identical. The average emission per area (bottom line of ST4) of 1.262 kg$\cdot$hr$^{-1}\cdot$km^{-2} applied to the 15,271 km^2 within the white boundary in figure SF5, or covered in figure 5 of the main article, would result in 19.3 Mg/hr.

If the mass balances of overlapping sub-regions A and B need to be combined there are always three types of areas involved: (i) the overlapping part, (ii) an area only in balance A, (iii) an area only in balance B. If we do not know where the CH_4 sources are positioned, it is not possible to make a meaningful average that is valid for the overlapping part. This can be shown by examples with the real emissions positioned exclusively in (i), (ii) or (iii), and with combinations thereof. However, when we are using an emission inventory as a first guess in a relative way, we can calculate a meaningful average. As an example, BU(A)/TD(A) is 80 %, and BU(B)/TD(B) is 150 %. Then we apply the average of 115 % to the emissions in the overlapping area. Please note that this is not adjusting the TD estimate to BU, but only using the geographical information and the relative source rates.

The result of such an aggregation of the 32 sub-regions to one overarching TD domain is presented in figure 5 of the main article. This combined map is useful for identifying sub-regions where the BU inventory is systematically below or above the TD CH_4 emission estimate. The caption to figure 5 must be read carefully, and the map must not be over-interpreted.

The numerical results are listed in table ST6, including sensitivity cases, i.e. different results when different assumptions about CBL, trajectories, etc. are applied. The numerical results in ST6 are a reliable summary, but the hard information is in the 32 sub-regions, where TD and BU estimates can be compared directly (figure 4 in the main article, and tables ST4 and ST5 below). The results in figure 4B are discussed further in the main article.

The only direct emission approximation for the full TD domain is determined by adding the mass balances bal_16_1 and bal_16_2, according to figure SF10 (the red boundary in this figure and the white boundary in figure SF5 or SF6 are comparable; both contain the two CSG clusters). These alternative estimates for the emissions within the full TD domain are listed as additional cases in table ST6.

H Characterisation of the vertical profiles

As mentioned in section B, vertical profiles were flown before the first and after the last transects. Additional soundings between the transects were flown if possible within the available flight time (active CBL). Figure SF18 is showing an example of profiles that are showing the top of the CBL relatively clearly. This was not the rule. Quite often, only the TKE-profile was specific, and the other methods discussed below for assessing the CBL height became important. All the overviews for the complete flights are available as electronic supplements (section F).

I How we determined CBL heights (mixing heights)

CBL: Convective Boundary Layer. Within the CBL, all constituents in the air (trace gases such as CH_4, H_2O, CO_2, and sensible heat) are mixed vertically within less than an hour. During the campaign, i.e. during spring in Queensland, the top of the CBL typically reached between 2,000 and 3,000 mAMSL (1,700 to 2,700 mAGL) in the late afternoon. The flights usually started shortly before noon, when the CBL was at least reaching 1,000 mAGL and surface inversions and residual layers were eroded already. Then the CBL grew during the observations (see SF20). The last transect was usually flown around the time of the maximum temperature at about 4 p.m. (no later than 5 p.m.), avoiding the complex evening transition of the CBL.

The vertical soundings allowed us to identify the top of the CBL with an accuracy of about 100 m. The criteria used were the thermal stability (neutral within the CBL, ideally topped with a stable layer as visible in figure SF18), the mixing ratios of water vapour, CO_2, CH_4 and aerosols, and – most useful – the turbulence as TKE profiles. Since the latter has no 'memory', i.e. there are no 'residual layers of turbulence', this turned out to be the best parameter. Also, the observations by eye, and the real-time data on the screen in the cockpit allowed us to assess the CBL altitudes during the flights. The visual observation of the top of the dust layer is the main reason why we are assuming, that CBL tops were relatively flat (discussion below), rather bound to an altitude above sea level [m AMSL] than a height above ground [m AGL].

The soundings could only deliver single values every one or two hours at specific locations. However, there are options to estimate the CBL top continuously along the transects. One possibility is offered in cases where shallow cumulus clouds formed on top of the CBL. For those four days, a strict thermodynamic process was used to deliver a continuous estimate for the CBL altitude along the transects. Within a CBL, i.e. in a neutral layer, the rising pockets of air are cooling dry-adiabatically at about 10 K/km, whereas the dew point decreases by about 2 K/km (more precision see on thermodynamic diagrams such as a 'skew-T-log-p-diagram'). For example, when the in-flight measured temperature is 20 °C and a dew point is 10 °C, condensation happens about 1,250 m above the altitude of the flight. Even in dry cases, where no cumulus clouds were formed, this method yields an upper limit for the top of the CBL.

In dry cases or early phases of the day, where small convective clouds only formed later, another thermodynamic consideration was applied. When knowing the temperature at altitude, the top of the CBL can be calculated by using the measured temperatures along any flight track. Since not all the early soundings reached above the top of the CBL hours later (which was not ideal and is a lesson learned), the temperature profiles from the GFS analysis were used instead. Practically, we always used both data sources on one thermodynamic graph, where this 'third opinion' for a continuous CBL top was determined.

These two thermodynamic methods for the estimation of the time-dependent development of the CBL at the locations of the transects are shown in figure SF19 for a day that began with dry convection but cumulus clouds in the afternoon. Using the evidence from the analysis of the individual sounding profiles (section H) as well, a 'best guess' plus a lower and an upper limit for the CBL top can be determined. The three cases were applied to all the mass balances, i.e. the reference case was using the 'best' CBL top. A maximum emission estimate is calculated using the minimum CBL for the upwind leg (reduced column mass) and the maximum CBL for the downwind leg (increased column mass), whereas a lower limit for an emission estimate was achieved vice-versa. All these cases were part of a sensitivity analysis and hence a realistic error estimate for the sub-regional emission estimates and the total emissions for the TD domain (tables ST5 and ST6).

Rather for curiosity than as a fourth method we applied an own high resolution convection model to the area. Since this model is not yet published, it has no importance for our emission estimates. However, it challenges the subjective impression, that the CBL top was flat. The considerable structure in the CBL top in figure SF21 is reflecting the topography, and different albedo below the simulated CBL. Even if this structure is impressive, it is not dramatic for a mass balance as long as the transects are limited to a sub-region with moderate changes in terrain elevation, i.e. not across the basin (blueish CBL) and the hills (green, yellow, red). However, since we cannot be sure about the horizontal structure of the CBL top we used both options when calculating mass balances: Either a flat CBL top, or a terrain following top. The resulting differences are part of the sensitivity analysis expressed in tables ST5 and ST6. The CBL tops resulting from the empirical thermodynamic method (figure SF19) are including any effects of topography, soil moisture or albedo.

The important parameter for the mass balance is not the CBL altitude alone, but the volume between the surface and the top of the CBL. Even if we know the surface topography from the digital terrain model (SRTM in this study) at high resolution and accuracy, it is not directly clear which scale is relevant. It is certainly not the highest available resolution of about 100 m on the one hand, nor an average flattening hills and basins on the other. Since the 'columns of methane mass' we are dealing with are on a 1 km^2 grid, this is the lower limit for a reasonable horizontal resolution. We decided to smooth the topography further to 5 km, i.e. the surface elevation of each pixel is the average within the 25 km^2 centred around the pixel. Otherwise, any small hill would influence the mass balance, and the 5 x 5 km^2 are also in agreement with the grid from the Katestone inventory that was used when comparing TD with BU from UNSW and Katestone. Two sensitivity cases for the CBL development for the largest sub-region are shown in figure SF20.

It has to be emphasised that these two very powerful thermodynamic methods as well as using measured turbulence (TKE) for estimating continuous CBL tops require fast and accurate airborne measurements for temperature, humidity and turbulent wind, i.e. this is at least as important as a high stability for the methane measurements.

J How we determined background concentrations

At this stage, the most important question is, what the relevant background concentration was, or more precise, what the drift of the background concentration between the upwind and the downwind transect was.

In principle it would not be necessary to subtract a background concentration from the total concentration provided the density 'δ_M' in (eq. 5) could be perfectly measured, because (eq. 4) is valid for absolute column masses as well. However, as we are considering uncertainties in the measurement of the temperature in the order of 0.5 °C, and of 0.5 hPa for pressure, we end up with a relative uncertainty for the density in the order of 0.2 %. Applied to the absolute concentration of about 2 ppm, this corresponds to 4 ppb, i.e. about half the concentration differences between transects. This is the main reason for subtracting a background concentration for the calculation of column masses.

Another necessity for dealing with background concentrations is the vertical mixing from above the CBL. If the CH_4 concentrations above the CBL are lower than within the CBL (usual case), the CH_4

between the transects is diluted, i.e. the emissions from the surface would be underestimated. In the opposite case, with enhanced concentrations above the CBL (as found on all six days discussed here, visible for one day in figure SF18, lower left frame), the entrainment of a few ppb CH_4 from above would lead to an overestimation of the emissions if this contribution would be neglected.

This effect was included in the mass balances in two steps: The initial estimate for the drift of the background concentration between the first and the last transect was calculated based on the first sounding profile and the CBL growth thereafter, quantifying the contribution from the entrainment for all the transects. Additionally, minimum concentrations on the transects were manually identified and compared with the calculated evolution. Minimum concentrations measured after rapid descents from soundings were ignored because it seems that those minima were caused by non-homogeneous temperatures in the measuring cell. When established on transects, the temperature was stationary and the CH_4 readings reliable again.

Whenever the background concentration derived from the time-series was lower than the half-hourly estimate by the entrainment, the whole depth of the CBL at this time was adjusted to this new minimum. The measured minimum is dominating because it is based on evidence, whereas the mixing was a first guess, and is useful for the times in between the evident minima. The difference between the two is an indicator for the uncertainty of the background concentration during the day, which is caused by two processes: (i) Even if the initial profiles were taken on the upwind side of the sub-regions, they cannot discern lateral structures within it. (ii) The concentrations above the CBL (that are mixed downwards during the day) might not be constant horizontally as well.

The workflow described in section D guarantees that a downwind background is rather over- than underestimated (the minimum found might already be influenced by distributed sources) and hence the mass balances are rather underestimating the real emissions. Also, the fact that dry deposition or photochemical removal of CH_4 might exist but is not considered even over the very large areas, is leading to underestimations.

The trends in background concentrations found with this combined method were between -0.48 ppb/hr, and 1.26 ppb/hr (mainly positive), leading to a reduction of the emission estimates. Table ST7 is listing these values.

Conclusion: Especially when larger horizontal or vertical gradients in CH_4 concentrations in the incoming air mass are present, the background concentrations are an important factor for a mass balance on this scale, with concentration differences between up- and downwind of typically 10 ppb. Taking a conservative value for these observations of ±2 ppm/hr leads to a relative uncertainty in the mass balances of 20 %. About the same variation of results was found with the sensitivity analysis according to tables ST5 and ST6, where the influence of the entrainment to the background concentrations is already partly included.

Another important factor is instrumental accuracy. The absolute accuracy is not important as long as we do not compare or combine the concentrations with those from other sources. However, we must be sure that the instrumental drift is not larger than the uncertainty we have for the background concentrations. The empirical finding, that the minimum concentrations did not change more than 1.3 ppb/hr during each flight is indicating that the instrumental drift was also within this limit, which is well within the specifications of the LGGA[2]. It would be a big coincidence if during 9 flights, an instrumental trend would always have compensated for a larger background trend in the atmosphere. However, for future campaigns on such a large scale we should try to install an in-flight calibration (injecting periodically a stable concentration to the intake). A cross-calibration with the UNSW team has been made by analysing three SKC FlexFoil bag samples of 5 litres of calibrated Southern Ocean air (1.800 ppm certified by CSIRO) sent from Sydney to Adelaide. This improvised comparison was showing an offset of our LGGA (factory calibrated only) of 18 to 20 ppb but it was stable within these two values.

K Details about the wind field (trajectories)

Both in section B and in section E, air mass trajectories played an important role. Within this study, four types of trajectories were calculated: (i) forward trajectories from the two emission clusters based on GFS forecasts for the flight planning; (ii) backwards trajectories between the flown downwind

[2] https://www.lgrinc.com/documents/LGR_Ultraportable_GGA_Datasheet.pdf

transects and the upwind transects based on measured winds from the aircraft; (iii) checking trajectories according to (ii) against the GFS analysis; (iv) forward trajectories plus diffusion modelling for the reconstruction of the 4-d CH_4 mass distribution based on a detailed emission inventory (see section L).

All these trajectories were calculated based on a 2-d wind field on the altitude and time of the flight legs within the transects, either from GFS (0.25° lat/long resolution), or from the measured wind along the flights (120 seconds averages below 500 mAGL, i.e within the lower CBL). Since the airborne measurements were following first-guess trajectories already, the interpolation of the wind along the trajectories did not need a temporal component, i.e. the time was not a factor in the inverse square distance interpolation.

The absolute accuracy of the wind measurements during the flights is better than 0.5 m/s for the horizontal components (u,v). Hence, the offset of a trajectory (forward or backwards) after one hour travel time is in the order of 2 km (less due to measurement errors, but the wind field can vary in time and space). At low wind speeds as on 10th and 12th Sep, this can cause large uncertainties in the direction of the trajectories. However, this still means that the plume of a known source is crossing the flight track within ±2 km, or vice versa, a CH_4 peak in the measurements can point to a distant source with this lateral accuracy. As described later in section M, a distance estimate is also possible.

Another uncertainty of the interpolated trajectories is that we cannot distinguish between a temporal change of the wind (instationarity), or a change in space (inhomogeneity) along the flight. If the flight is quasi Lagrangian, this is not important. However, if the trajectory types (i) to (iv) from above were compared for the most critical day (16th Sept) with long trajectories, we believe that the ±2 km per hour travel time is a conservative error estimate.

Therefore, when a plume was found outside of this range for a known source, we are assuming that it is either an unknown source, or a 'ghost source'. Especially in the morning, plumes can creep in local wind systems along small structures in the surface before being mixed up in the growing CBL. The plume under discussion in figure SF6 (dark pink slices in the north-east), SF17 and SF24 was found during the afternoon in a well-defined wind field (figure SF6), i.e. the chance that this plume was offset by more than 3 km is low. Nevertheless, both options are possible: Either the plume was originating from an unknown source, or a known 'ghost source' was stronger than according to the emission inventory. Since, during the flight, we were convinced that the plume was originating from a well-known source, the remaining flight time was used for improving the spatial resolution across one transect. If there would have been any doubts, additional crossings could have been flown into the wind. Such single-source observations were made during a later campaign in October 2020.

Using different assumptions for the wind field is part of the sensitivity study reflected in tables ST5 and ST6 (reference case versus TD_Bi).

L The dispersion model MoDiM

(**Mo**nte-Carlo **Di**spersion **M**odelling): Emissions from known or supposed sources can be injected in the boundary layer by a Lagrangian particle diffusion model. We released particles carrying one gram CH_4 per hour (or more grams per particle when the emission rate was larger than 10 kg/hr, i.e. a maximum of 10,000 trajectories per source). This random walk for up to 10,000 trajectories per source randomly picked 3-d wind vectors (u,v,w at 10 Hz) from the nearest flight leg. After this initial diffusion, the plume widening was kept at a constant rate (lateral and vertical angle), because when proceeding with the random walk, the plume does not widen anymore, because all trajectories are tending to the average wind. In reality, at each point of the plume, a new diffusion begins. Since such an algorithm would explode, the approximation of constant plume widening after a certain distance was chosen in agreement with analytical descriptions of plumes in the atmosphere [SR3], [SR4]. The shorter the initial diffusion time, the wider the following linear plume widening. The time for the initial diffusion is the main parameter to control the MoDiM algorithm. It can be adjusted for each day (wind regime) if one or several plumes from known sources were crossed during the flights, allowing to adjust their widths to the measured width. After these adjustments, the initial diffusion times were between 60 and 180 seconds. Vertically, the height of the plume is limited by the CBL, i.e. after reaching the CBL top, the vertical mixing is asymptotically reaching perfect vertical mixing.

A similar dispersion model could be built using a Gaussian plume around the trajectories (sigma(x,y,z) for all the days were isotropic around 1 m^2/s^2). However, since we measured 3-d wind vectors at 10 Hz, the Monte-Carlo random walk was an interesting alternative, especially because we did not have to deal with concentrations but used particles of a constant mass.

With this method we got 4-d data blocks using the same 1-km-grid as described above (eq. 5) for the vertical integration of column masses (voxels of the dimension dx,dy,dz of 1 km x 1 km x 50 m). Using the molar density of the air along the flight tracks, concentrations based on the particle mass in a voxel can be calculated and compared with the measured concentrations. The main benefit of MoDiM is an overall picture of the 4-d distribution of methane mass (primary) or concentration (secondary) that can be used for several purposes (example in figure SF22). It is important to note that the usefulness is not depending on details of the algorithm, because it is mass conserving. Plumes can just grow faster or slower laterally and vertically, but the flux through any cross section will not change.

The 4-d data blocks are memorising the three most relevant emission sources for each voxel, i.e. the algorithm is ranking the mass contribution of each source to each voxel, keeping the three most important ones. When the virtual flight is crossing voxels with enhanced concentrations, these smaller or wider peaks can be labelled with the number of the source that is responsible for the peak in the model. Even if a similar peak in the measured concentrations might be slightly offset, the measured peak can be associated with this source.

MoDiM is offering a complete 4-d picture based on a chosen emission inventory which can be compared with the measurements in many ways. Three options are discussed below. In addition to the quantitative methods based on MoDiM it allowed to visualise any emission scenario as shown in figure SF22.

M How MoDiM was used for an independent emission estimate

The forward dispersion modelling (MoDiM) offered a second method for sub-regional emission estimates and for individual plumes. Starting with zero emissions or a first-guess emission inventory one can adjust both the distributed sources and the point sources in a way, that the simulated concentrations along the flight track are corresponding with the measured concentrations. One advantage is, that assumptions like the perfect vertical mixing are not necessary. This is especially important when relevant sources are closer than about 10 to 20 km to the downwind transect (less than half an hour mixing time, which is not sufficient to reach the top of the CBL). The prime disadvantage of this method is, that it is very time-consuming because it is a manual iterative process, especially for the reconstruction of the upwind conditions (sources (1) to (17) in figure SF23). Therefore, only one day was reconstructed using this method. The diagnostic tool for the iteration is a combined plot of the measured and simulated concentrations with the dominating source numbers, allowing to assess and adjust all the considered sources. Such a graph for a complete emission field as shown in SF23 is too complex to be shown here. However, figure SF24 is showing a smaller example to illustrate the method. In principle, the concentration measurement along any flight track could be analysed with this method, delivering emission estimates for the upwind side.

N How MoDiM was used for assessing possible errors in the pure mass balance

As already mentioned above, MoDiM can be used to assess the extent of the vertical mixing between any source of CH_4 on the surface until it reaches a flight track. Even if the model cannot simulate all the details of a convective boundary layer, where e.g. one single thermal can pick up emissions near the surface and transporting them with 2 m/s or faster up to the top of the CBL, it can show average conditions based on the measured turbulence. A key parameter derived from the 10 Hz 3-d wind vectors is the average vertical turbulent mass flux that was quite robust around 0.5 m/s (ranging from 0.51 to 0.66 m/s for the seven days). This means, that the complete exchange of mass (mixing) is proceeding with about 0.5 m/s. These conditions were found to be quite isotropic, i.e. perfect mixing is widening with about 0.5 m/s both horizontally, and vertically. These empirical 0.5 m/s can be taken as a lower limit for the plume widening both vertically, and laterally, i.e. it takes less than 4,000 seconds to reach a CBL top on 2,000 mAGL. The fastest pockets of air are reaching it within less than 1,000 seconds, while the Lagrangian particle dispersion model is also quantifying the range in between.

Having this information about a simulated vertical CH_4 mass distribution on any transect for any source is allowing to assess the error that is made by the assumption of perfect vertical mixing within the CBL. The result of such an assessment was, that in most cases the pure mass balance was within 90 to 110 % of the simulation, i.e. the assumption of perfect mixing under these conditions, in sufficient distance from the major sources, is acceptable. The perfect mixing assumption can both under- and overestimate the real or the simulated flux (i.e. the column mass in the downwind wall) because the measurements can either be made on an altitude, where the concentration was less than the average concentration in the CBL, or vice versa. When assuming enhanced concentrations near the surface (which is not always the case – see section P with figure SF17), slightly decreasing with height, an underestimation of the flux is most likely when flying "too high", while flying "too low" could result in overestimation. However – once again – it must be noted that the absolute column masses are less important than the difference between up- and downwind. Therefore, if a chosen height of flying is resulting in a systematic over- or underestimation of column masses, the difference might still be accurate.

The fact that the comparison of the perfect mixing assumption agreed well with the simulation confirmed, that a height of 150 to 300 m above the surface was a good choice for the given meteorological conditions.

The same considerations as for the vertical plume widening can be made for the horizontal plume widening. Looking in more detail into the relative position of major sources and transects showed, that non-ideal conditions in the horizontal are more frequent and more important than in the vertical. Figure SF25 is explaining the consequences when an end of a downwind transect is cutting relevant plumes. In other words, the area of a sub-region is not sharply defined, i.e. there can be some cross-talk to neighbouring emissions, or emissions within the sub-region that are not fully accounted for. Smaller sub-regions are more exposed to these effects than larger ones. Therefore, when sub-regions were split (as shown by three examples in figure SF6) this was done along slices with low emissions.

O How MoDiM was used for characterising peaks and bag samples

Initially, MoDiM was developed for backwards trajectories from positions on the flight tracks, where CH_4 peaks or bag samples should be connected to possible sources (footprints). An example is given in figure SF26. However, it turned out, that the forward dispersion modelling of all the known sources, with their projection on all the flight tracks, was more successful for the identification of CH_4 concentration peaks and for the characterisation of bag samples.

P An example of an individual plume

When flying on the long downwind transect on 16th Sept, a distinct plume about 30 km north-east of Dalby was detected. After the second crossing on the way back, four additional crossings at different heights were flown, and bag samples were taken. This excursion and the concentration peaks are visible on the figures SF6 (the pink slices in the north-east), on SF10 (north-east of the blue sub-region 'bal_16_10') and on figure SF17 (cross section). Four methods were used to quantify the emission rate of this unknown source: (i) A detailed two-dimensional mass balance along the vertically resolved transect as described in [43 (main article)] estimates 2.7 Mg/hr; (ii) the mass balance bal_16_10 with 3.4·Mg/hr, and (iii) with 2.4·Mg/hr (for both see table ST4, column 'TD_ref'); (iv) the fit according to section M and displayed in figure SF24 suggested a source emitting at least 2 Mg/hr in about 30 km distance. Please note that only (i), using the two-dimensional information about wind and concentrations on the transect has the highest accuracy of about 10 %, whereas (ii) and (iii) are based on the assumption of perfect vertical mixing up to the top of the CBL, while (iv) using the dispersion model MoDiM (section L) is simulating the vertical mixing to some extent, however, only decreasing with altitude, i.e. it cannot reflect the concentration maximum 300 m above the surface. Two conclusions are possible with this example: (a) Even with the limitations shortly mentioned for (ii) to (iv), a rough estimate for the emission rate of individual sources is possible from single crossings by making the assumption of perfect vertical mixing under suitable meteorological conditions, and (b) the accuracy of these estimates is increasing with distance (allowing enough time for mixing) as long as the concentration enhancement is sufficient for the precision of the instrumentation and the knowledge about the conditions (CBL top and background).

Q An outlook on measuring vertical turbulent transport instead of advective fluxes for emission estimates

While evaluating the best method for a top-down emission estimate for a larger region by airborne measurements, another approach was checked: When measuring the evaporation of water from a surface, or the deposition of CO_2 to forests or other vegetation, the measurement of the vertical turbulent fluxes is the established method.

The technique of measuring vertical fluxes of CO_2, water vapour, and sensible heat is well established and important in meteorology [SR5], [SR6]. These turbulent fluxes or 'eddy covariance fluxes' are written as ‹c'w'›, where c' is the deviation of a scalar (trace gases or heat) from an average, and w' is the deviation from the average vertical wind speed, i.e. in most cases over flat terrain the vertical wind speed itself. Without going into details of the technique, these quantities were measured during our flights as well.

The premise for using such measurements for closing the mass balance is that if these vertical fluxes are known, the horizontal mass balance can be restricted to the height at and below the flight tracks, i.e. to a layer below 300 mAGL or even lower when the flights are performed at a lower height. All variations of CH_4 concentrations above this level could be ignored. There is no doubt that such a concept is theoretically sound and would work, provided these vertical fluxes can be captured with a sufficient accuracy and coverage.

Since w, CO_2, H_2O, and sensible heat were measured sufficiently fast (at 10 to 20 Hz) we tested the concept using these constituents. Both the vertical fluxes for CO_2 and H_2O showed reasonable values and patterns, i.e. more CO_2 deposition and evaporation of water above bush than above dry soil. The flux of sensible heat was in perfect agreement with the GFS model (where all surface parameters and the radiation budget are included), delivering values of about 300 W/m^2 during the flights. However, the vertical fluxes of CH_4 were obviously too low, i.e. the sum of the horizontal flux below 300 mAGL and the vertical flux was unrealistically low and showed large variations. We can identify two main reasons: (i) The measurement of the CH_4 concentrations was not as fast as for the other constituents (0.5 Hz or less; at least 1 Hz would be necessary for resolving important eddies of 100 m size); (ii) the transects did not cover the whole areas but were by design focussed on the borders of the areas under study. Since the emissions of CH_4 are much more structured than the sources for heat and water vapour, or the sinks for CO_2, the coverage of the region by such measurements was not sufficient. The flight patterns were not designed for applying this method.

Even as this approach was not yet successful, we should not forget about it for future campaigns. As soon as the CH_4 measurements are getting faster than 1 Hz we should try modified flight patterns over suitable sub-regions. The advantage would then be that flying could mostly consist of horizontal tracks in the lower boundary layer, with reduced priority for occasional vertical soundings. Also, meandering flights along plumes would be useful for this method.

R Supplementary figures SF1 to SF27

Supplementary material for Neininger et al., 2021, Comparing airborne TD emission estimates for methane against BU emission inventories for the Surat Basin, Australia,
Phil. Trans. R. Soc. A. doi: 10.1098/rsta.2020.0458

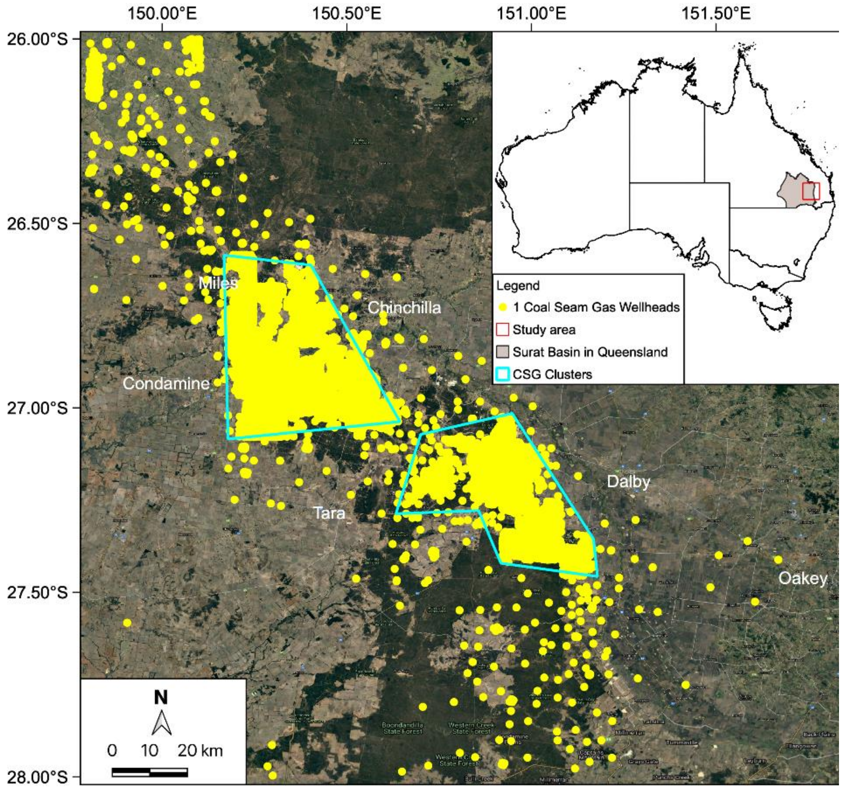

SF1: Coal seam gas wells in the south-east Surat Basin study area (category 1 in table ST1).

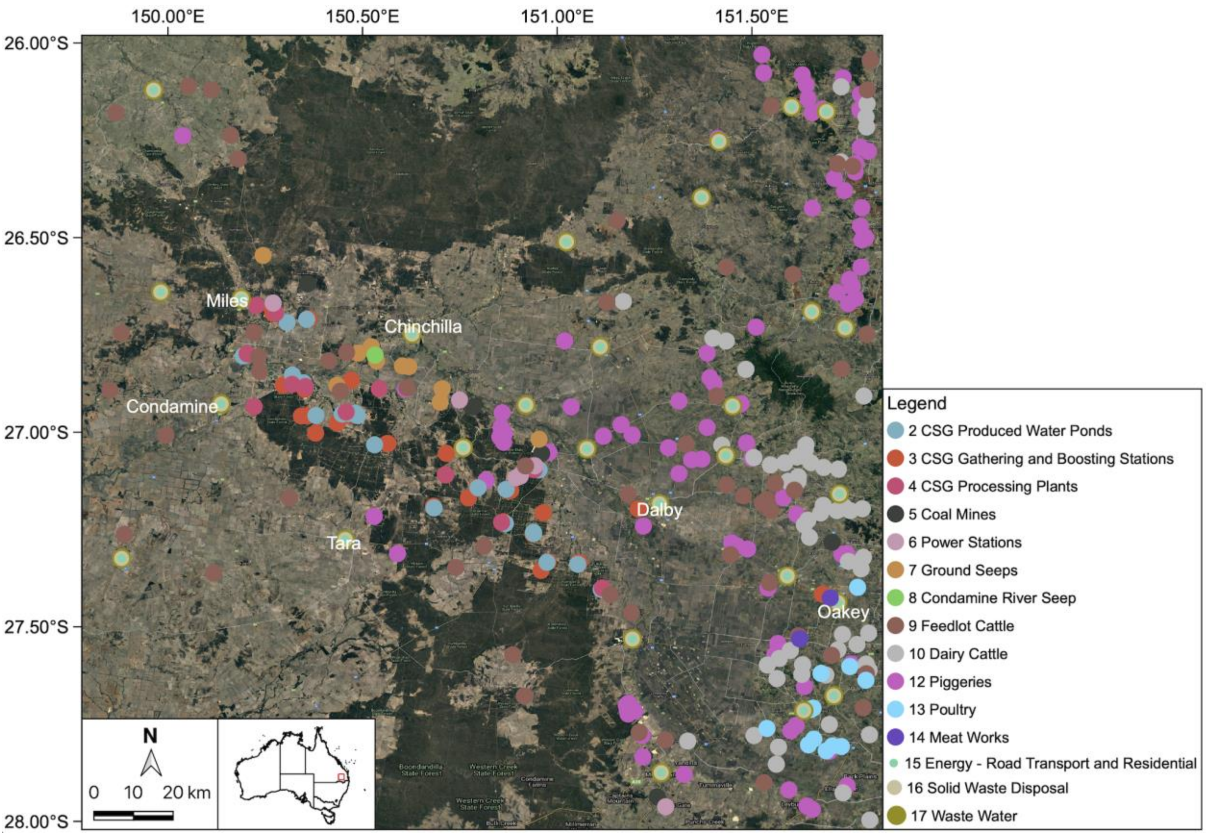

SF2: Methane point sources in the south-east Surat Basin study area (categories 2 to 16 in table ST1).

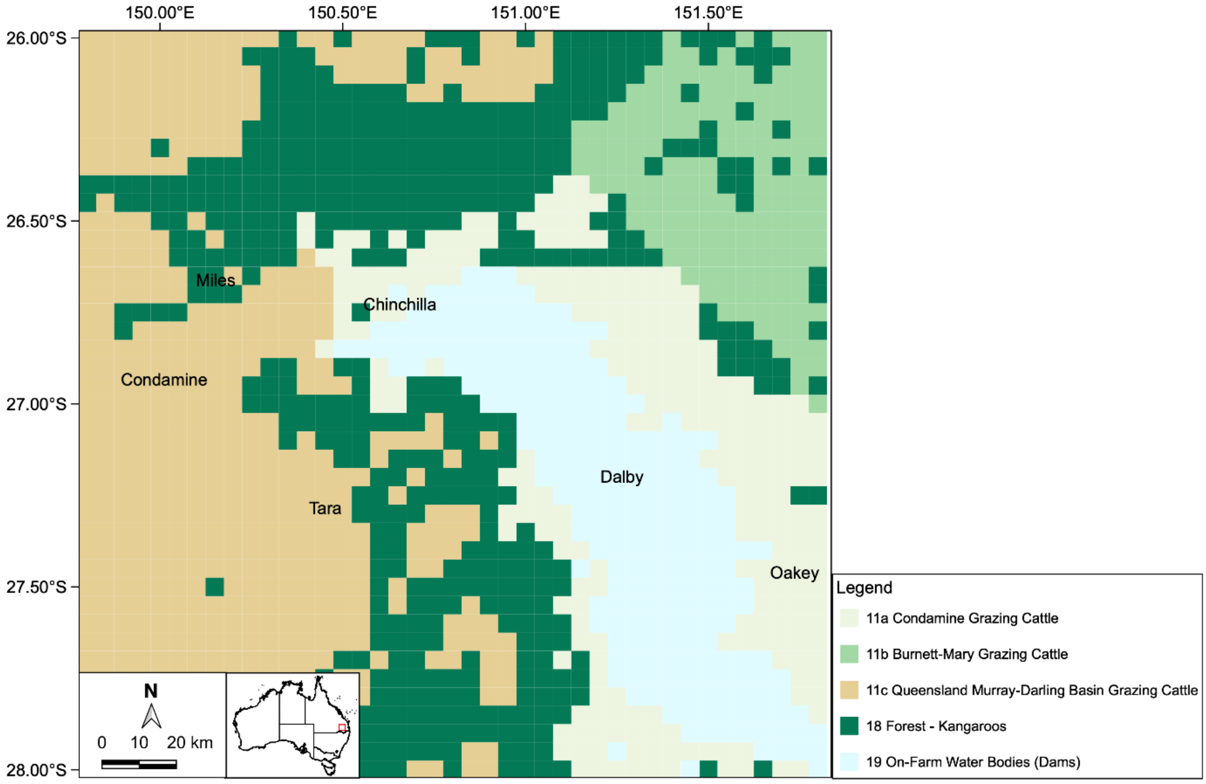

SF3: Distributed methane sources in the south-east Surat Basin study area (categories 17 to 21 in table ST1).

SF4: Left: The ARA research motorglider. Right Top: The ARA MetPod with the 3D-turbulence probe, the MetAir-modified LiCOR LI-7500 (mounted internally) and the MetOne particle counter mounted on one of the wing pylons. Right Bottom: The Los Gatos Gas Analyser and its external pump.

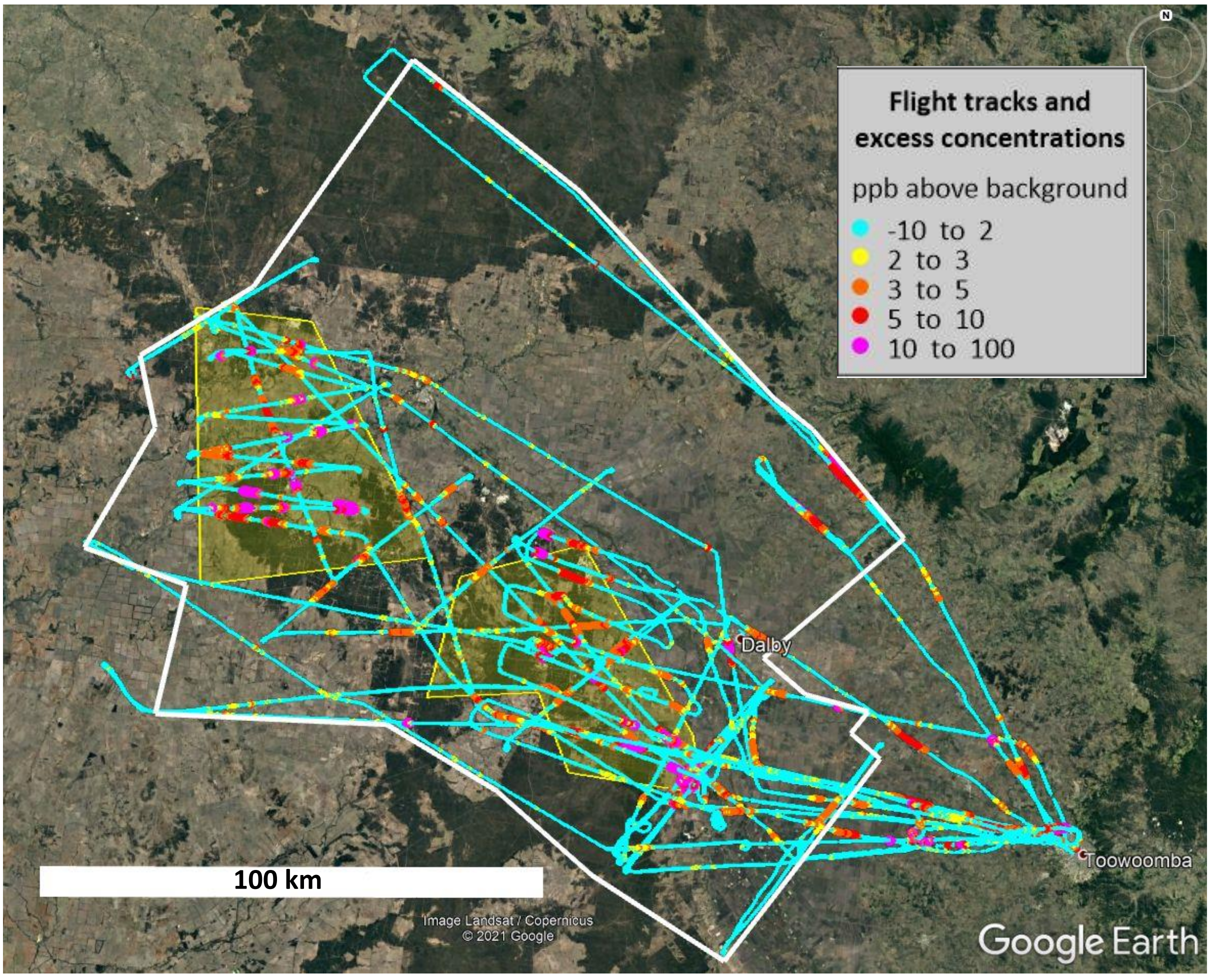

SF5: All flight tracks flown in the Surat Basin between Toowoomba in the south-east to Miles in the north-west during six days in September 2018 (only those flights used for mass balances). See the individual flights in the following figures, and in the electronic supplement (section F). The colours on the tracks are showing CH_4 concentrations exceeding the 10-minute moving average on these tracks, depicting individual plumes. The yellow shaded polygons are marking the two main clusters with CSG activities (summarising SF1). The aggregated emission estimates according to table ST6 and figure 5 (main article) are for the full TD domain within the white boundary.

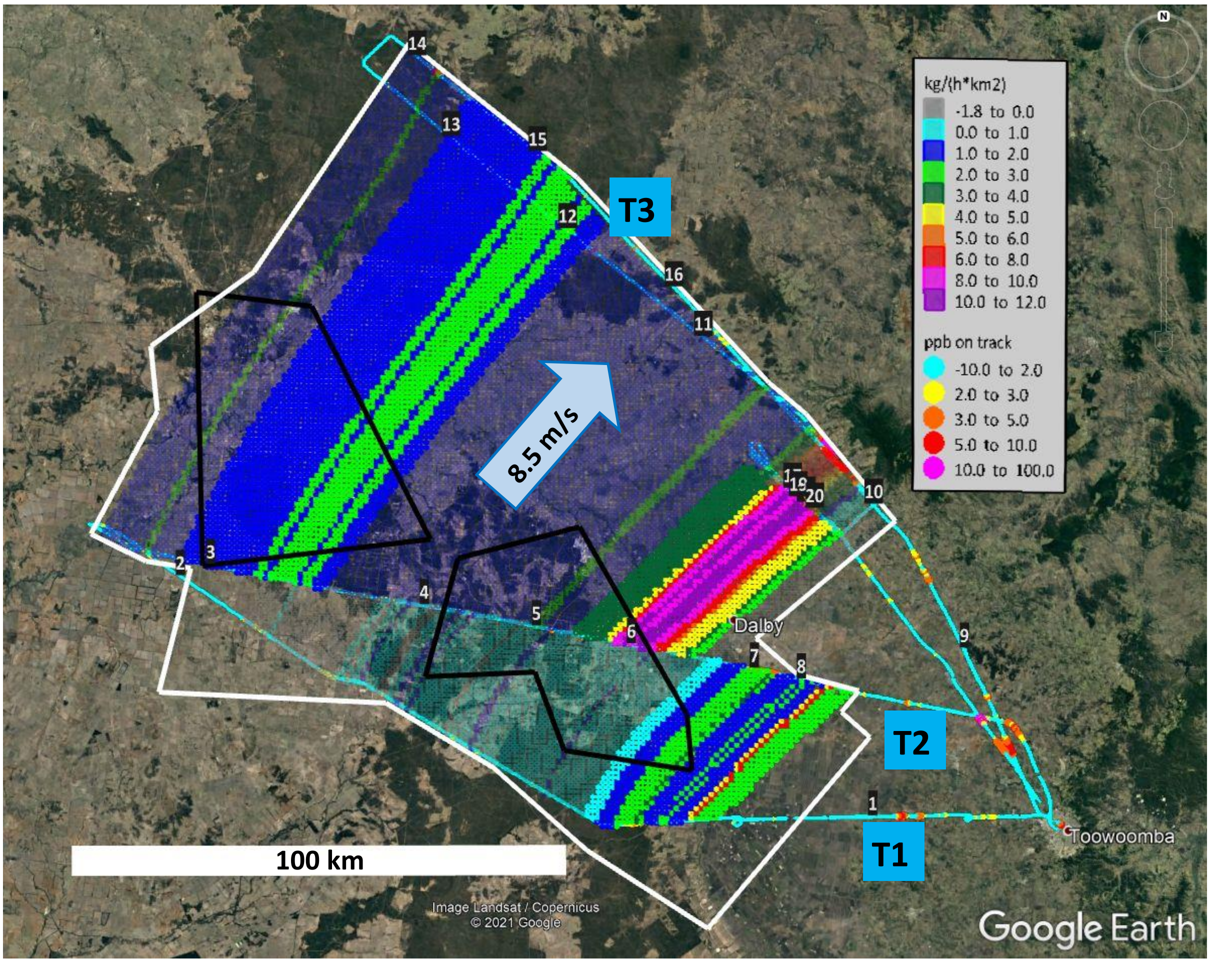

SF6: Explaining primary and secondary sub-regions (see SF10 for the naming of the sub-regions *bal_16_1* to *bal_16_10* for 16th Sept). The black polygons are marking the two CSG clusters. The large faintly colour-shaded primary sub-regions between the transects T1 and T2 (*bal_16_2*) and between T2 and T3 (*bal_16_1*) are covering almost the full TD domain (same white boundary as in SF5). Three examples of split sub-regions *bal_16_5* within *bal_16_2*, and *bal_16_7* and *bal_16_10* within *bal_16_1* are shown with stronger colouring. The green groups of slices in two of these secondary sub-regions and the pink group in the third are identifying CH_4 plumes. However, the distance of their sources from the transects is unknown. The white numbers on black are marking bag-fillings, i.e. the CH_4 in these bag samples (see section C) is characteristic for the associated sub-regions. The results of all the mass balances for this and the other five days with mass balances are listed in table ST4, and the coloured slices for each individual sub-region are available as kmz files for Google Earth (see section F).

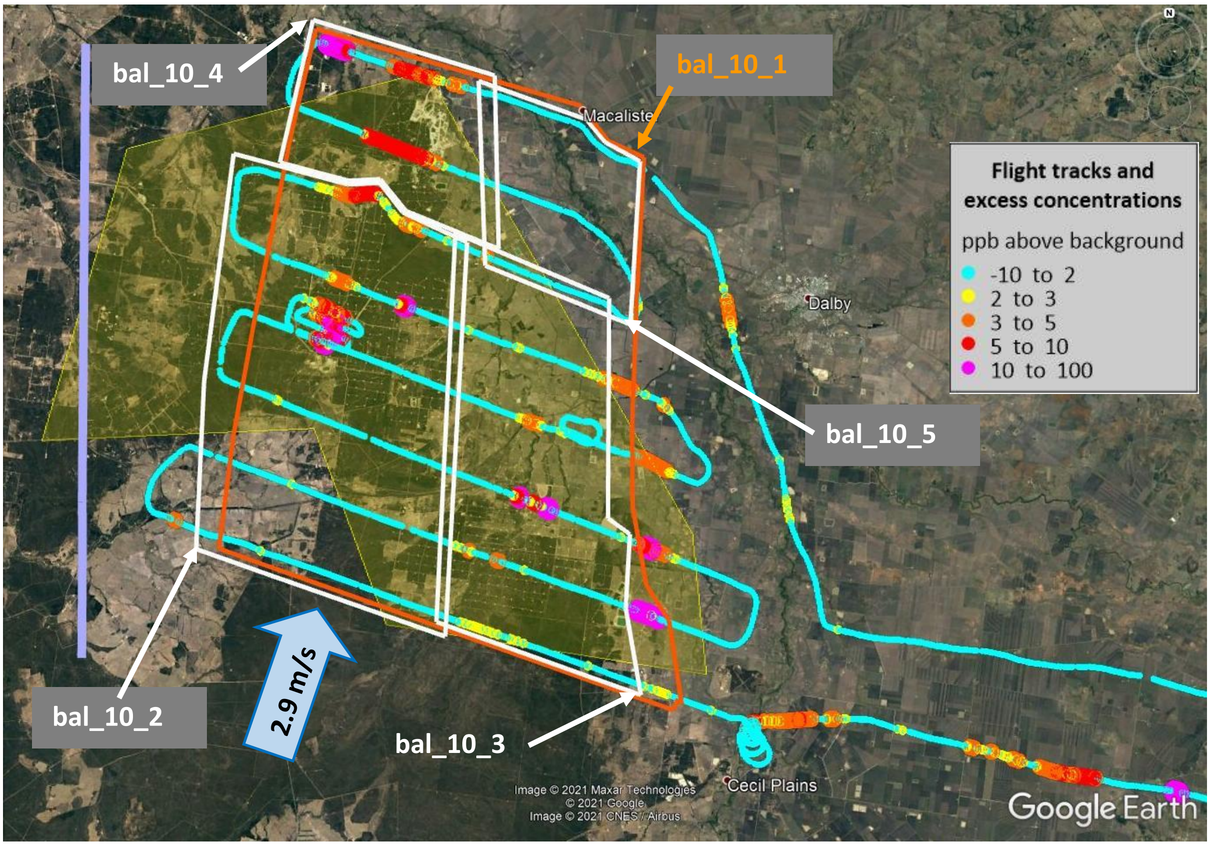

SF7: Flight track (non-Lagrangian raster pattern at about 150 mAGL) above the south-eastern CSG cluster (yellow shaded polygon) with colour coded CH_4 concentration peaks for 10th Sep 2018, 10:45 – 14:43 LT including ferry time. Four sub-regions are roughly outlined (precise areas see individual kmz in the electronic supplement F). The blue arrow is indicating the average wind. The grey vertical line on the left is 50 km long.

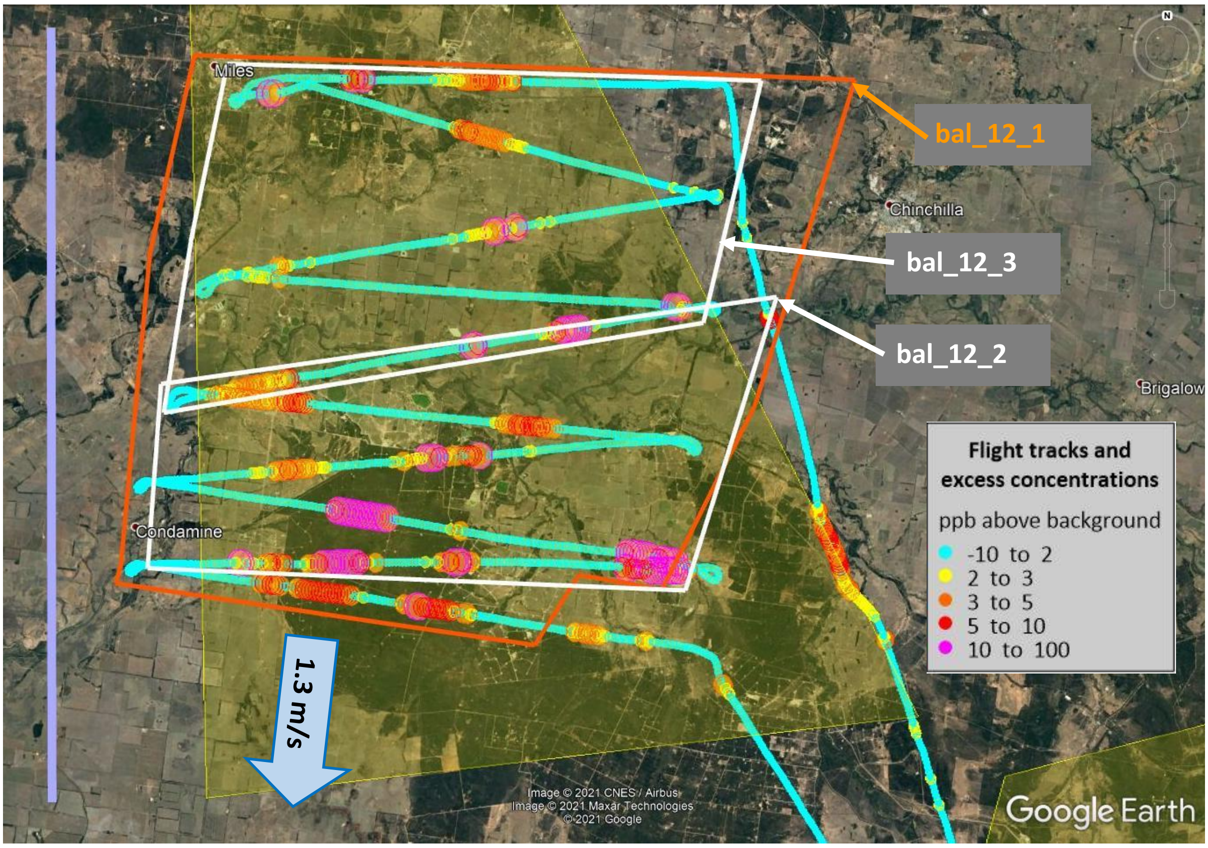

SF8: Flight track (non-Lagrangian raster pattern at about 150 mAGL) above the north-western CSG cluster (yellow shaded polygon) with colour coded CH_4 concentration peaks for 12th Sep 2018, 11:11 – 16:08 LT including ferry time. Three sub-regions are roughly outlined (precise areas see individual kmz in the electronic supplement F). The blue arrow is indicating the average wind. The grey vertical line on the left is 50 km long.

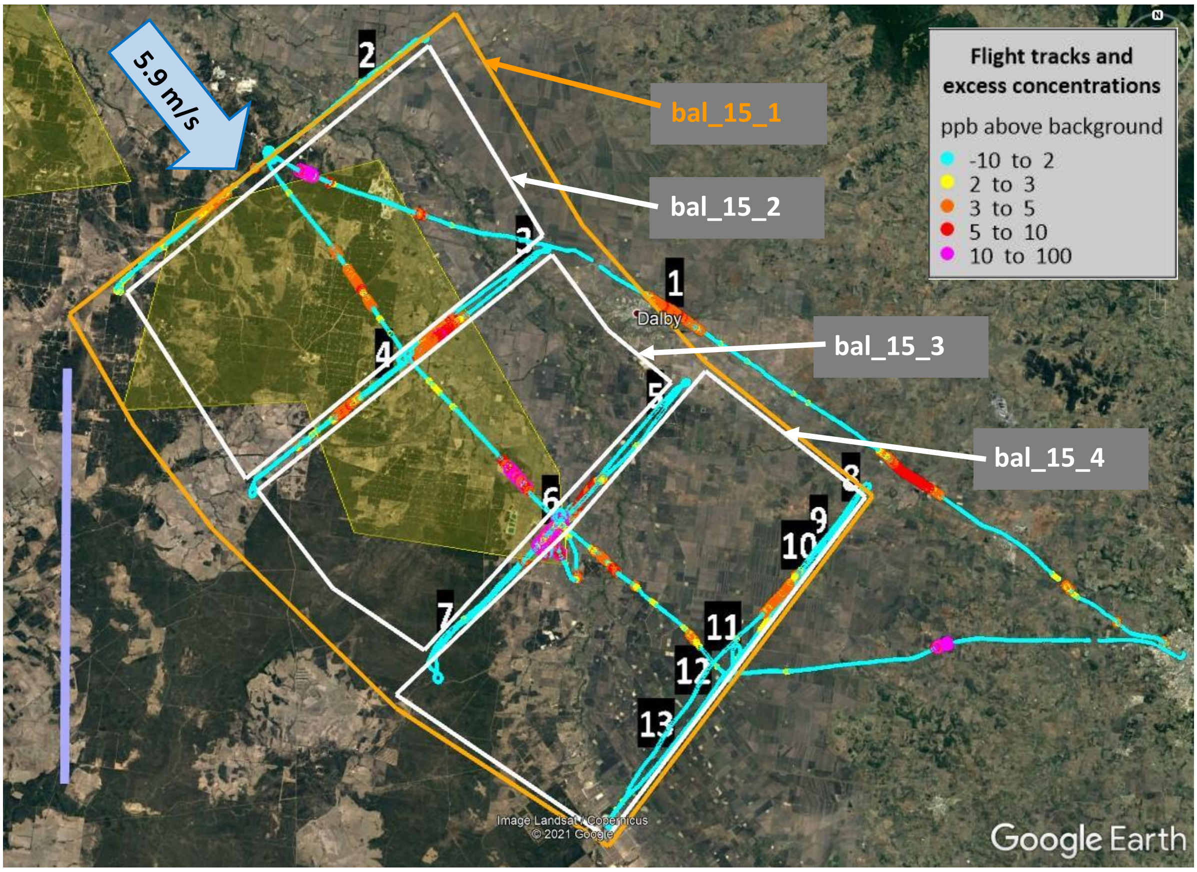

SF9: Lagrangian flight track along the basin at 150 and 300 mAGL above the south-eastern CSG cluster (yellow shaded polygon) with colour coded CH_4 concentration peaks for 15th Sep 2018, 10:17 – 15:11 LT. Four sub-regions are roughly outlined (precise areas see individual kmz in the electronic supplement F). The blue arrow is indicating the average wind. The grey vertical line on the left is 50 km long. The white numbers on black are marking bag samples.

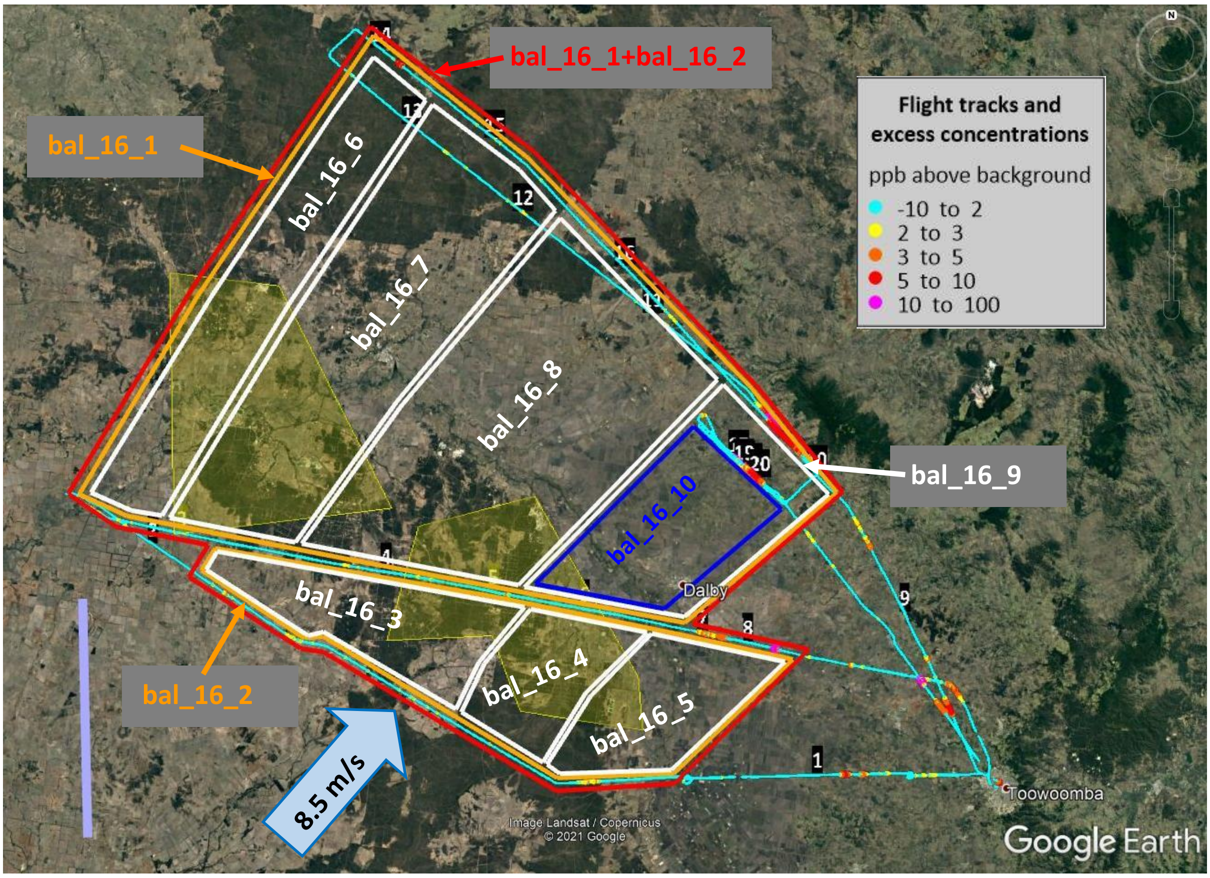

SF10: Lagrangian flight tracks mainly at 300 mAGL for wind crossing the basin, capturing both CSG clusters (yellow shaded polygons) with colour coded CH_4 concentration peaks for 16th Sep 2018, 09:30 – 16:39 LT (2 flights with refuelling in Toowoomba). Ten sub-regions are roughly outlined (precise areas see individual kmz in the electronic supplement F). The blue arrow is indicating the average wind. The grey vertical line on the left is 50 km long. The white numbers on black are marking bag samples.

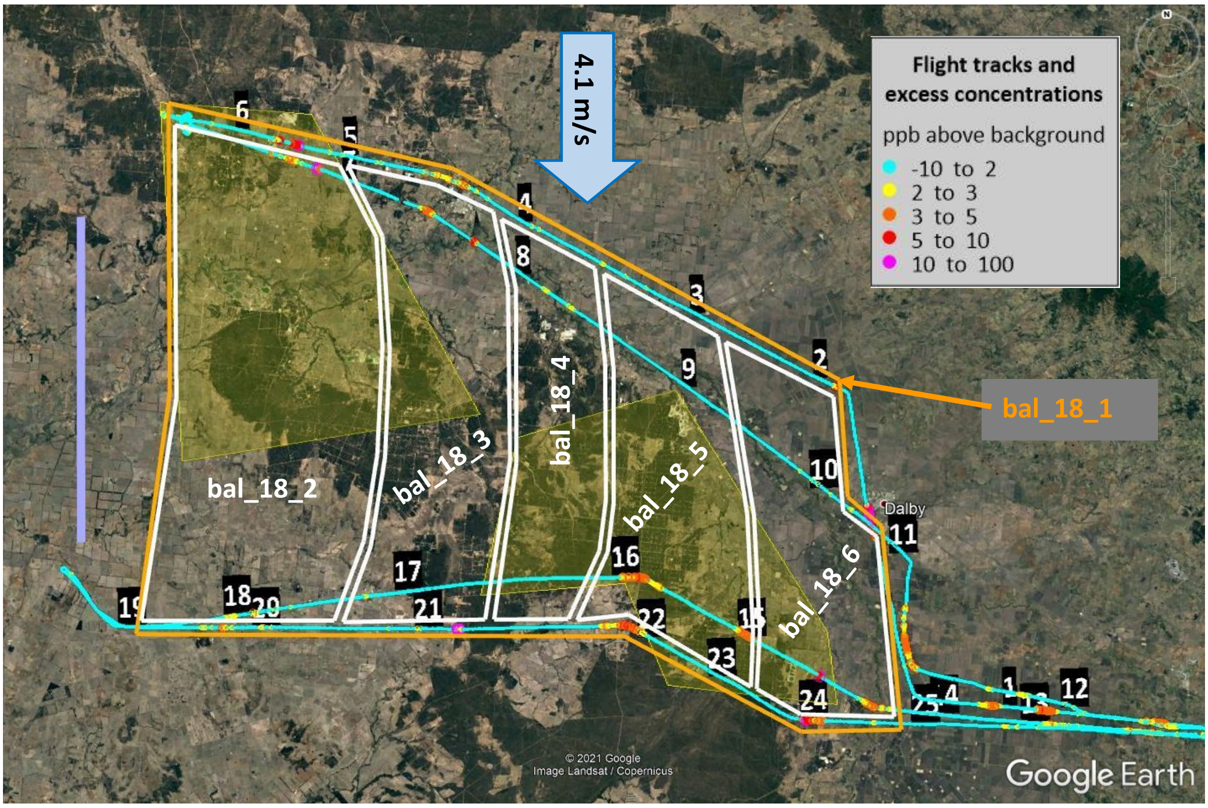

SF11: Lagrangian flight tracks mainly at 300 mAGL for wind crossing the basin, capturing both CSG clusters (yellow shaded polygons) with colour coded CH_4 concentration peaks for 18th Sep 2018, 09:42 – 16:06 LT (2 flights with refuelling in Toowoomba). Six sub-regions are roughly outlined (precise areas see individual kmz in the electronic supplement F). The blue arrow is indicating the average wind. The grey vertical line on the left is 50 km long. The white numbers on black are marking bag samples.

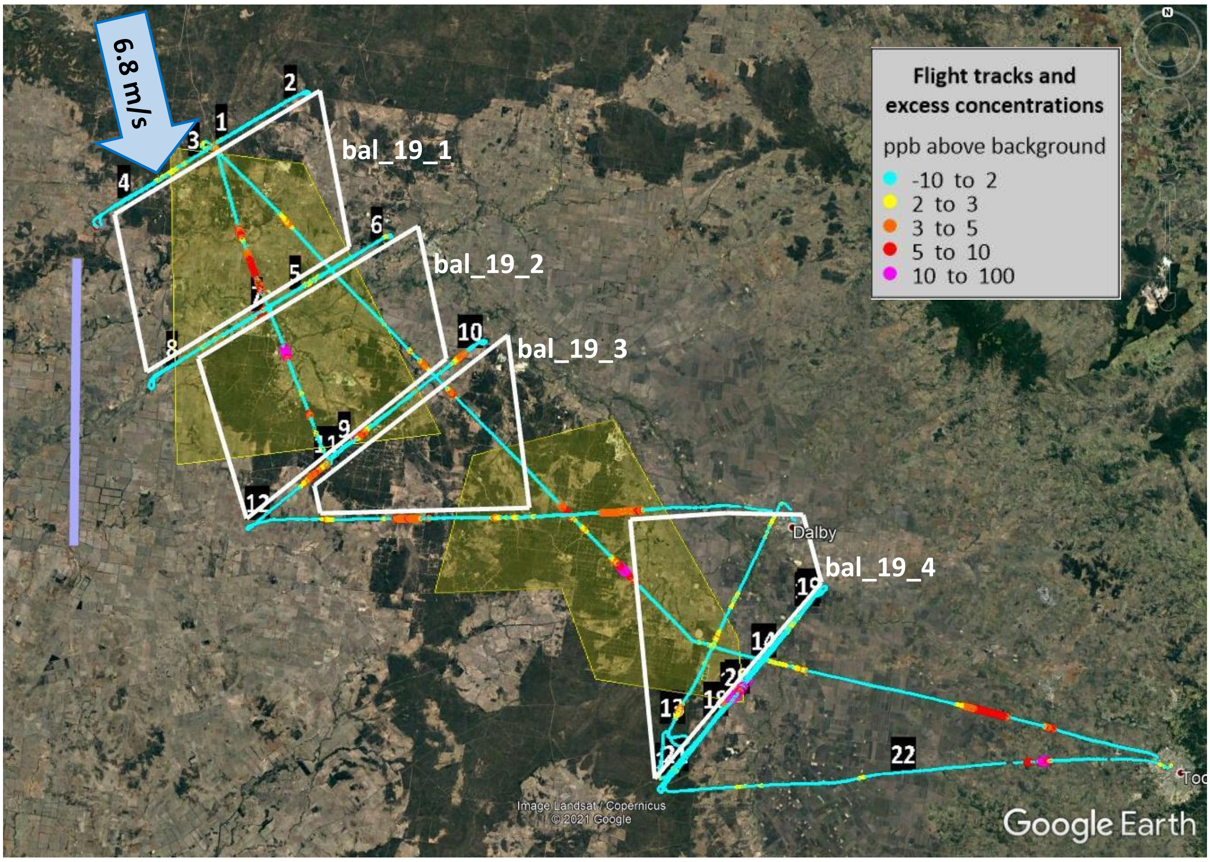

SF12: Lagrangian flight tracks along the basin at 150 and 300 mAGL above both CSG clusters (yellow shaded polygons) with colour coded CH_4 concentration peaks for 19th Sep 2018, 09:50 – 16:19 LT (2 flights with refuelling in Dalby). Four sub-regions are roughly outlined (for precise areas see the individual kmz files in the electronic supplement F). The blue arrow is indicating the average wind. The grey vertical line on the left is 50 km long. The white numbers on black are marking bag samples.

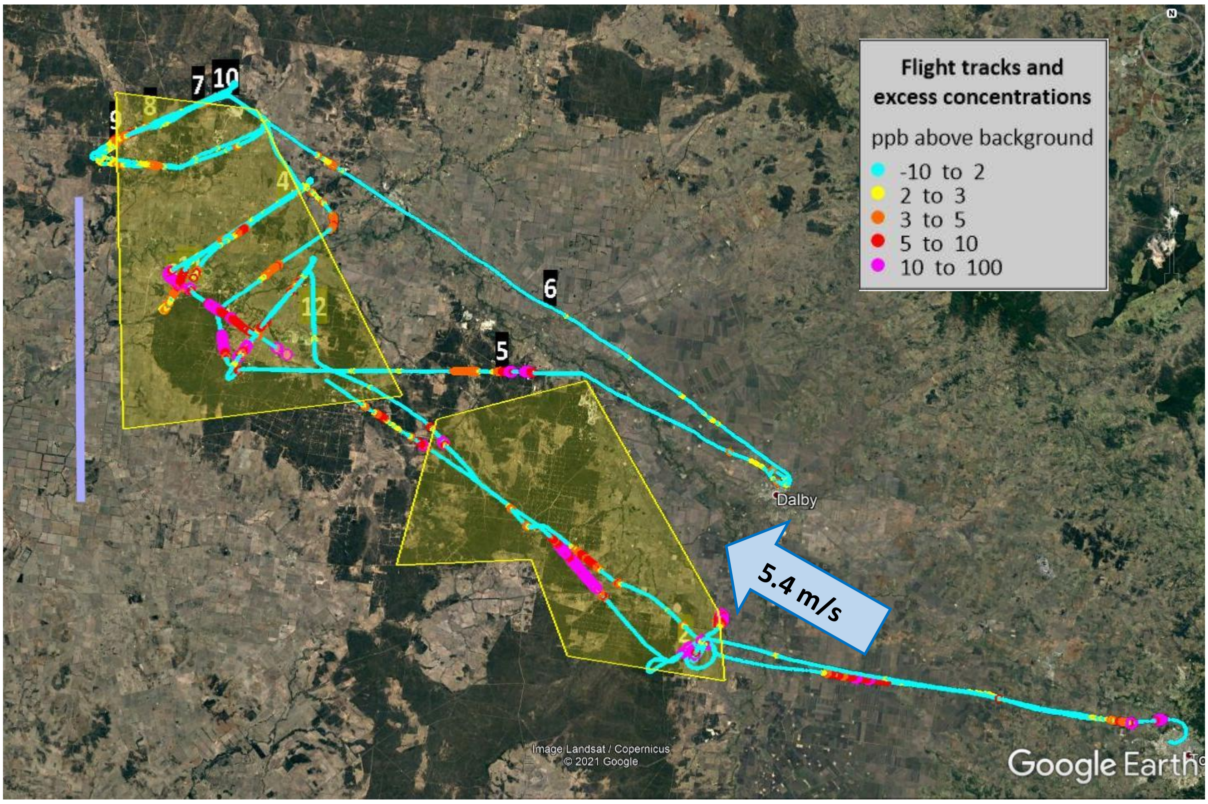

SF13: Non-Lagrangian flight tracks (2 flights with refuelling in Dalby) with colour coded CH_4 concentration peaks at mainly 150 and 300 mAGL for 21st Sep 2018, 09:15 – 16:20 LT with a focus on some individual sources in the north-western cluster (both CSG clusters marked with yellow shaded polygons). The blue arrow is indicating the average wind. The grey vertical line on the left is 50 km long. The white numbers on black are marking bag samples. This flight was not used for mass balances.

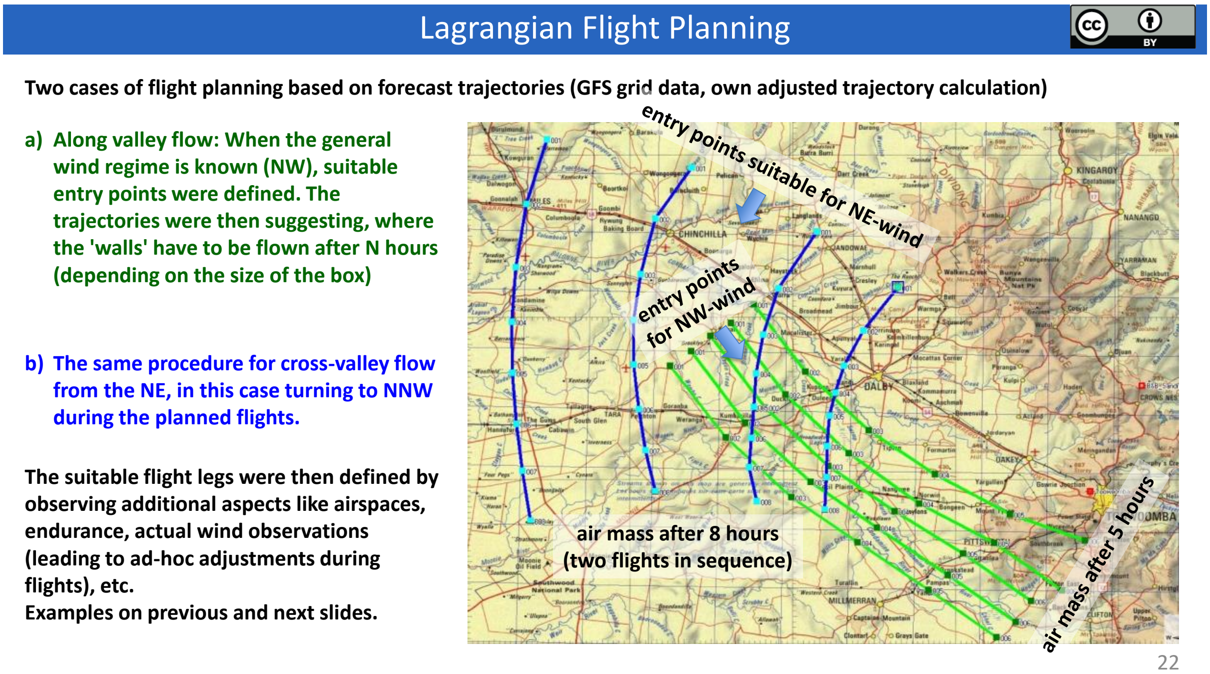

SF14: Trajectories calculated from GFS grid data (24-hours-forecasts). Based on these, suitable flight tracks were designed for getting Lagrangian transects.

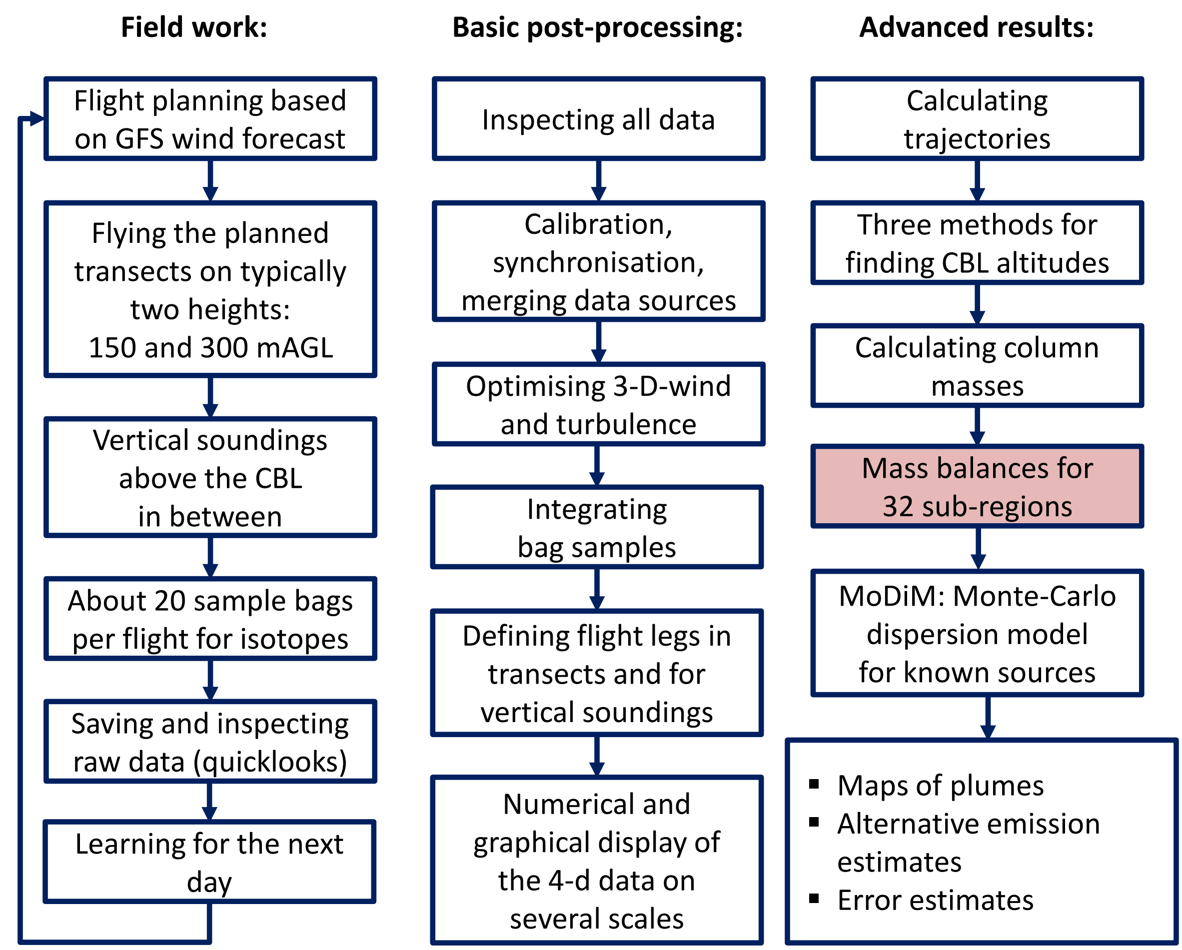

SF15: Workflow from the measurements to the results.

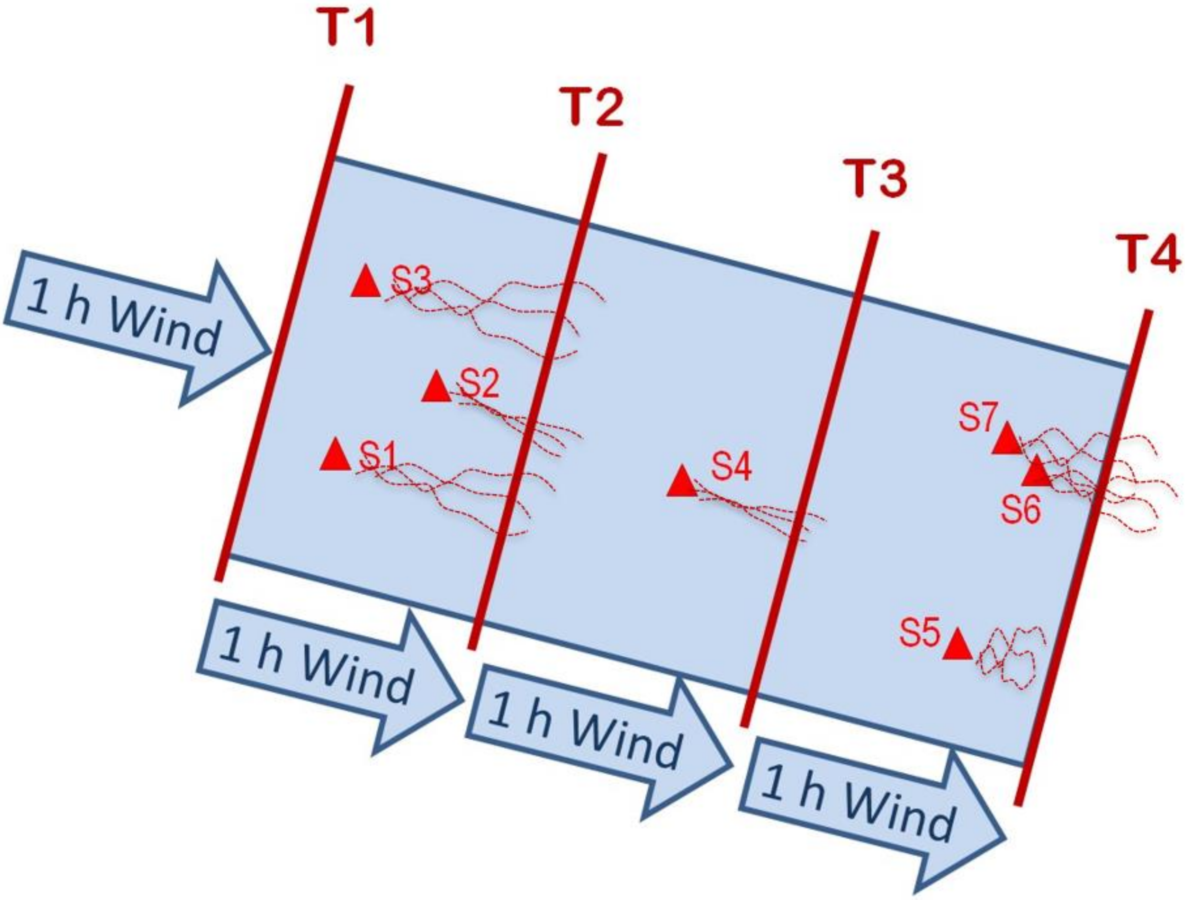

SF16: In this 2-d-view from above into the box, the air mass is moving from left to right, starting at transect T1, arriving three hours later at T4. The accumulated CH_4 is enhancing the average concentration at T4 compared to T1 or could even remain constant when the height of the box (i.e. the vertically mixed volume of air) is growing (see section I). The relevant quantity is the mass of CH_4 between the surface and the top of the imaginary box in the 'walls' along T1 and T4 (see section E). Within the sub-boxes between T1 and T2, etc., sub-regional emissions can be seen. When flying along the transects, the plumes from individual emission sources S1 to S7 are captured as well.

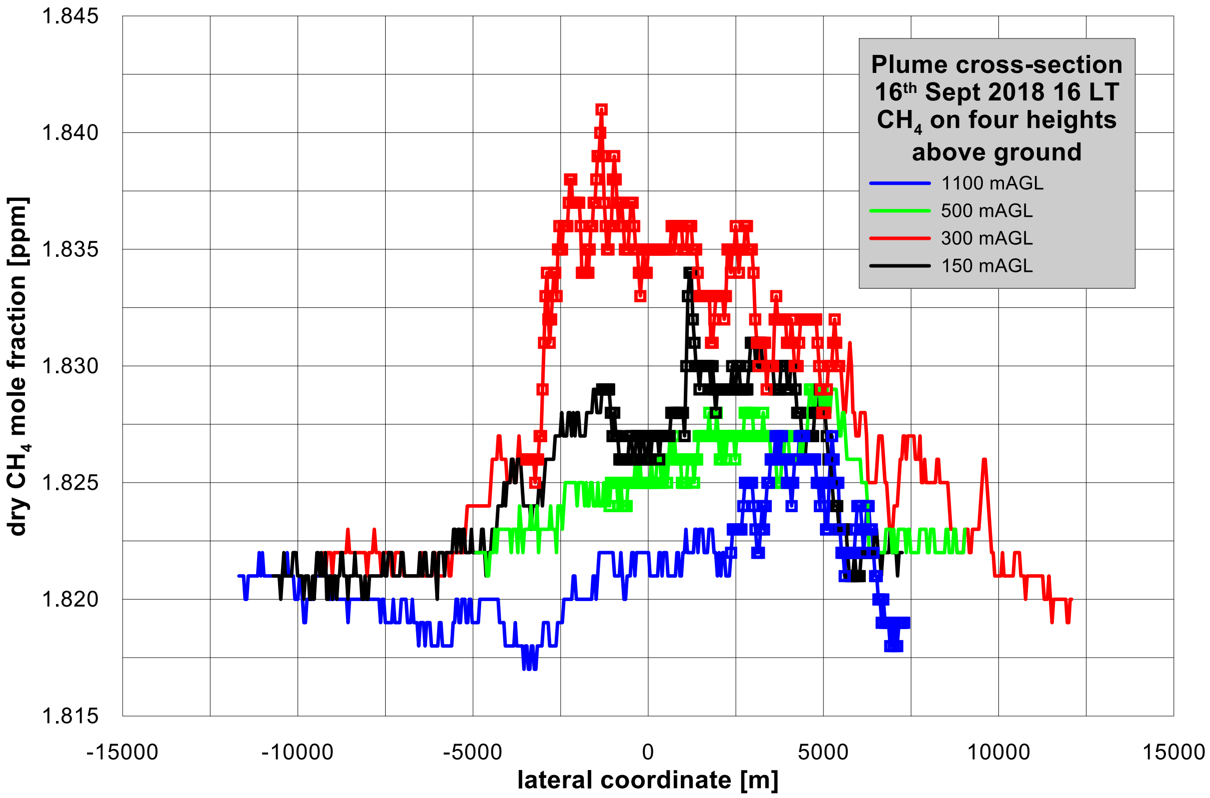

SF17: Crossing a plume about 30 km north-east of Dalby yielded these concentration patterns across the plume that had a width of about 10 km. The squares on the lines are marking the phases of bag fillings (see section C). The maximum CH_4 concentration was at 300 mAGL (red crossing), whereas below and above, the concentrations decreased. A calculation based on the wind field with the method presented in [43 (main article)] led to an emission estimate from the unknown source of about 2,700 kg/hr. Additional estimates are discussed in section P.

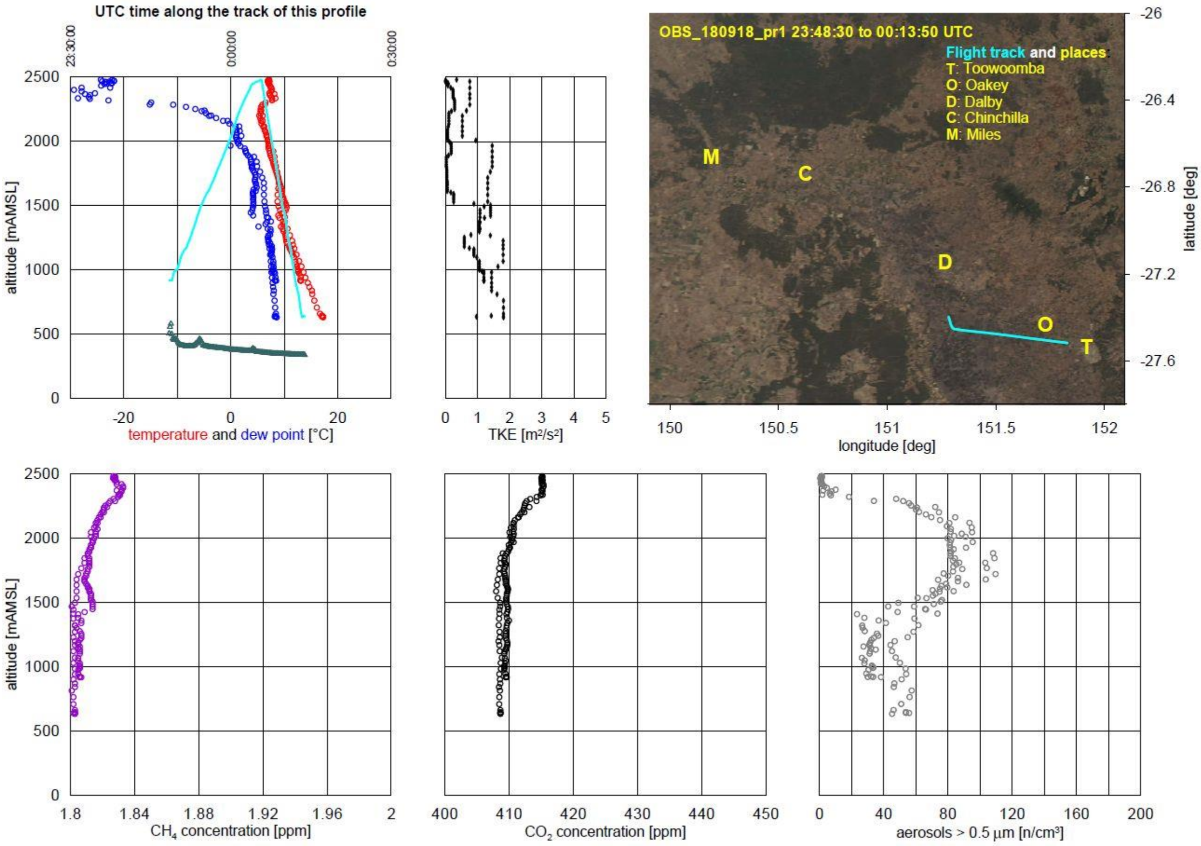

SF18: A working graphic right after the campaign, where the flight tracks and all the vertical profiles were inspected. Up to four vertical soundings per flight were performed. This example is showing the first sounding on 18th Sept during the ferry flight from Toowoomba to the first upwind leg. It was chosen because the top of the CBL is reflected in all six parameters. All soundings of the campaign are in the electronic supplement F. Top left: The time series of the ascent and descent (scale on top) for the altitude of the flight (light blue), the terrain, and the vertical profiles of temperature (red) and dew point (blue) using the bottom scale. Top middle: The vertical profile of turbulence. Bottom: The vertical profiles of CH_4, CO_2 and aerosols. Discussion see sections H and I.

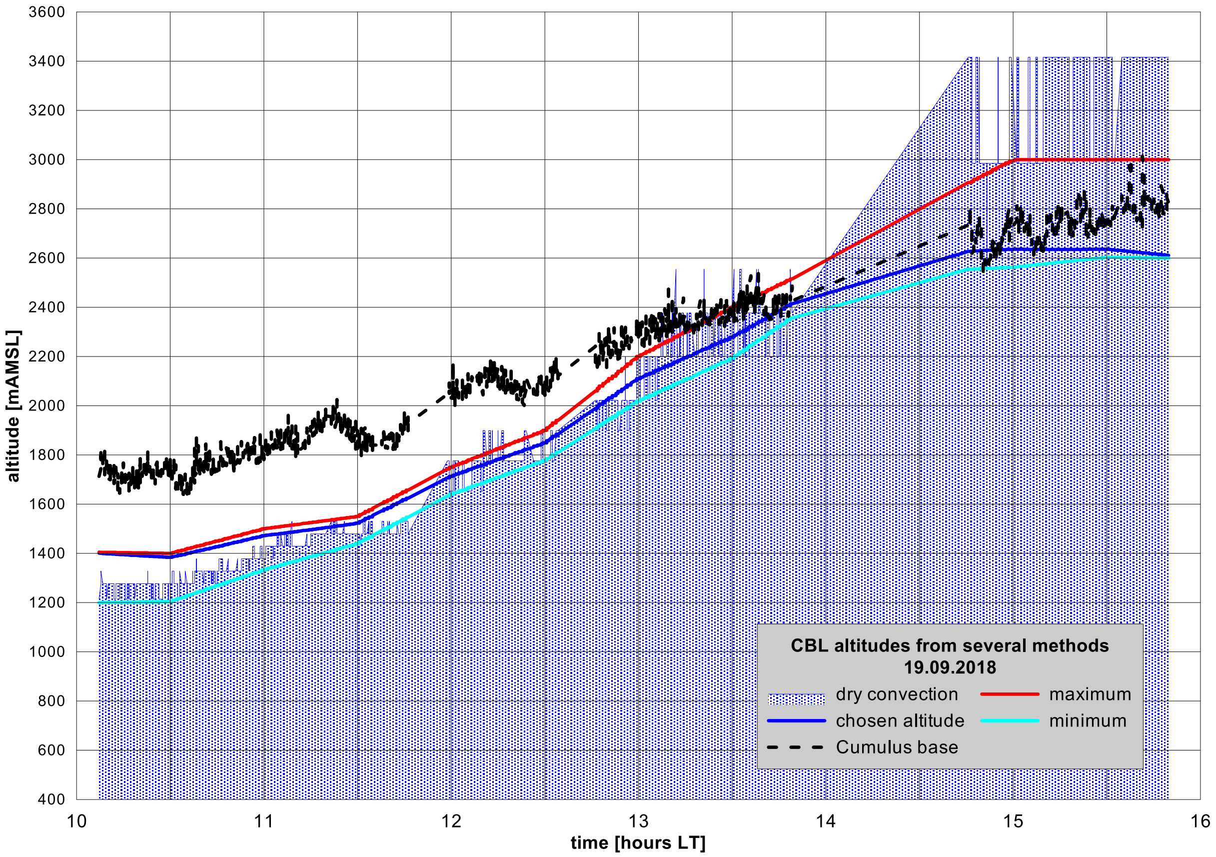

SF19: CBL height (as altitude above sea level) from several methods on 19th Sept 2018. The black dashed line marks the level where the cloud base would be found when cumulus clouds develop, based on the difference between temperature and dew point along the flight. The shaded blue with a thin blue line on top is depicting the result of the 'dry convection scheme' that needs some knowledge about the temperature around the CBL top. The light blue line and the red line are indicating the minimum and maximum altitudes resulting from all available information, including the evidence from the few vertical profiles. The blue line beginning at the maximum (red) at 1,400 mAMSL at 10 LT and ending at the minimum altitude (light blue) of 2,600 mAMSL at 16 LT is showing the 'minimum scenario' for a sensitivity case that is explained in the text and listed in tables ST5 and ST6.

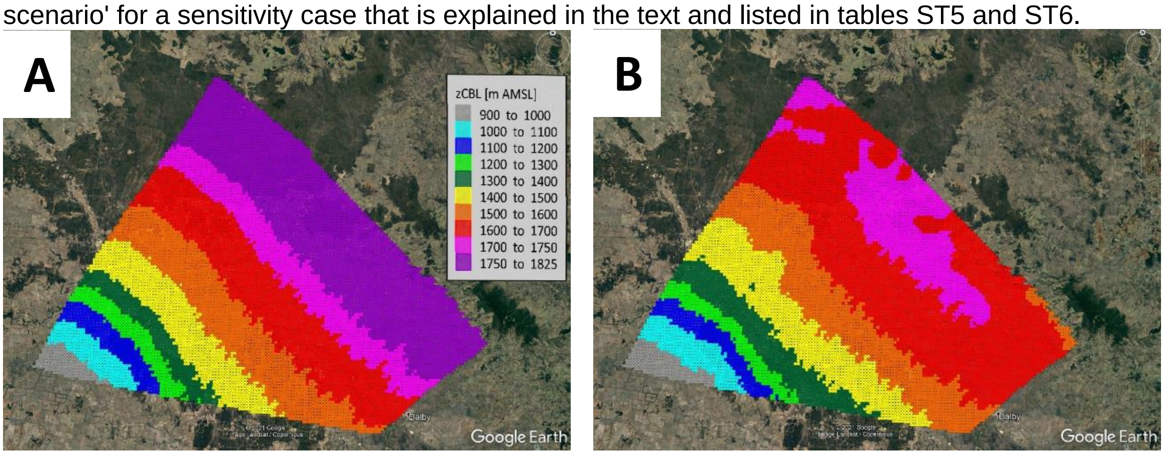

SF20: An example of the CBL height (as height above the surface) used for the mass balance *bal_16_1* (largest sub-region of the campaign, see figures SF9 and SF6). **A)** The top of the CBL is following the terrain, i.e. it is only depending from time (growing from about 1000 to about 1800 mAGL during the afternoon, i.e. between the upwind transect and the downwind transect). **B)** The top of the CBL is defined by the altitude above sea level [mAMSL]. Method B was used as standard, whereas A is one of the sensitivity cases shown in tables ST5 and ST6.

Supplementary material for Neininger et al., 2021, Comparing airborne TD emission estimates for methane against BU emission inventories for the Surat Basin, Australia,
Phil. Trans. R. Soc. A. doi: 10.1098/rsta.2020.0458

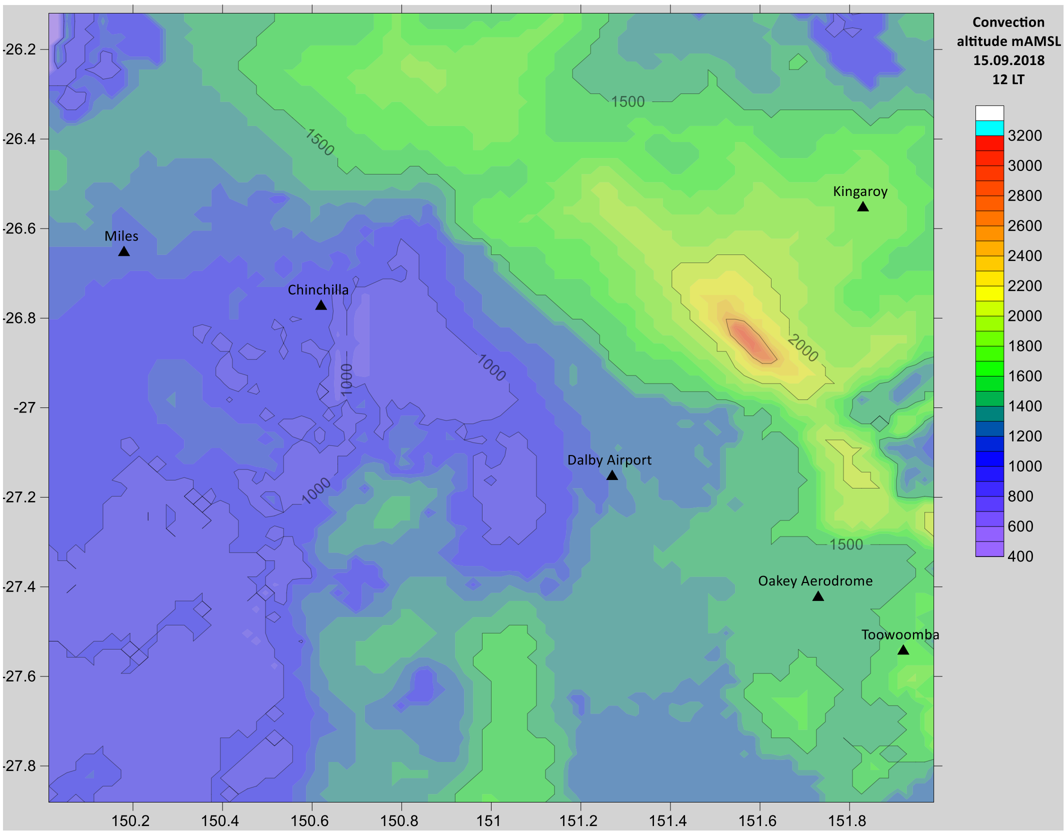

SF21: The structured top altitude [mAMSL] of the CBL as computed by a high-resolution convection model for around noon on 15th Sep. The difference between the Surat Basin and the hills north-east of Dalby is quite pronounced. Later in the day, these differences flattened (not shown here).

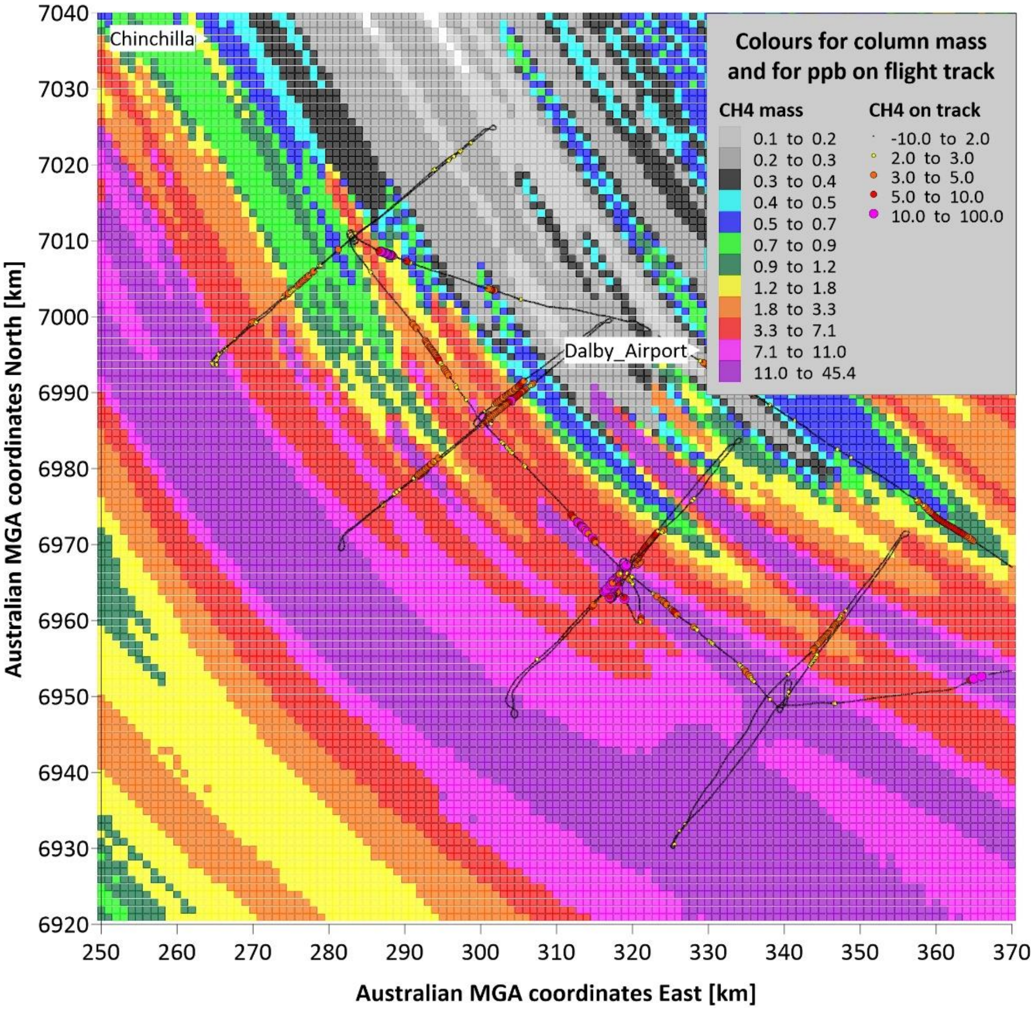

SF22: Calculated column masses over the Surat Basin based on forward modelling (MoDiM according to section L using the emission rates (kg/hr) from the sources specified in the UNSW emission inventory (figures SF1 to SF3 and tables ST1 to ST3, explained in the main article). The measured concentration peaks on the flight track are shown as well (see e.g. the yellow and orange on the last transect in the south-east, nicely correlating with the calculated plume). This flight from 15th Sept and the associated mass balances are shown in figure 2 of the main article, and here in figure SF9 above. Even when the modelled 4-d CH_4 mass distribution might not perfectly reflect the reality it is obvious that this information is useful for estimating the mixture of sources in bag samples (section C), or for identifying possible sources that caused CH_4 peaks along the flight track. Please note, that this model is not used for the mass balance calculations. They are exclusively based on the measurement. The applications of the model are explained in sections M through O.

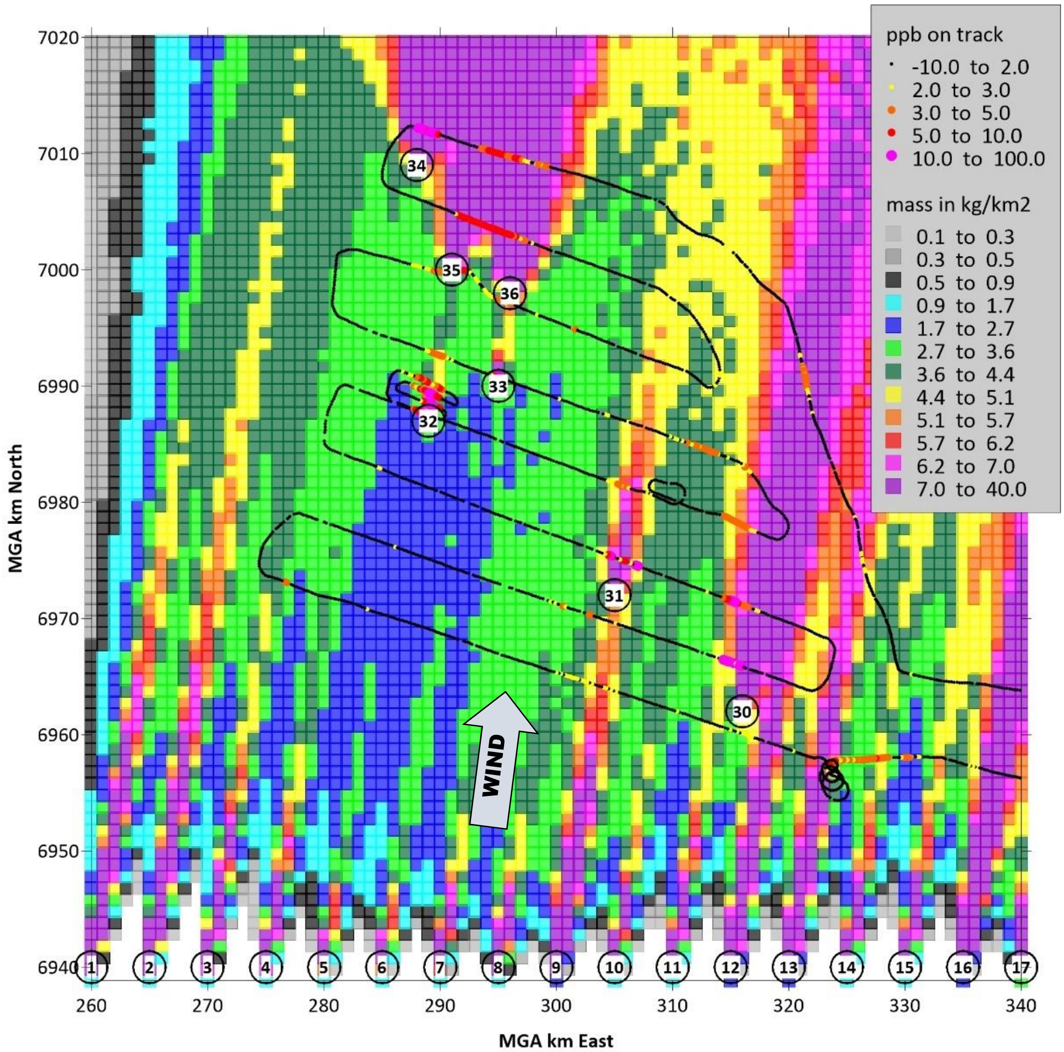

SF23: Column mass distribution in kg CH_4 per km^2-pixel and flight track with colour-coded peak concentrations for 10th Sept 2018. This mass distribution is not derived from the emission inventory (i.e. not like the example in figure SF22), but from iteratively placed virtual sources no. (1) to (36), fitting the measured time series of the measured concentrations along the flight track. After this time-consuming procedure, the sum of the virtual emitters (30) to (36) within the sub-region can be compared with the pure mass balance *bal_10_1* (figure SF7) from table ST4, and with the UNSW emission inventory: The total of the virtual sources for the fit is 1,980 kg/hr, the UNSW inventory estimated 1,452 kg/hr, and the range of mass balances from the sensitivity study is 1,392 to 1,699 kg/hr with the reference case at 1,572 kg/hr, and the median at 1,544 kg/hr. Additionally to the mass balance for the sub-region between the up- and downwind transect, this method is also delivering an estimate of upwind emissions (sources (1) to (17); (18) to (29) are east of this sub-region) of 3,915 kg/hr.

The iterative adjustment of the emission estimates

Working graph: Comparing the measurements with the dispersion model, allowing iterative adjustments of the underlying emission inventory

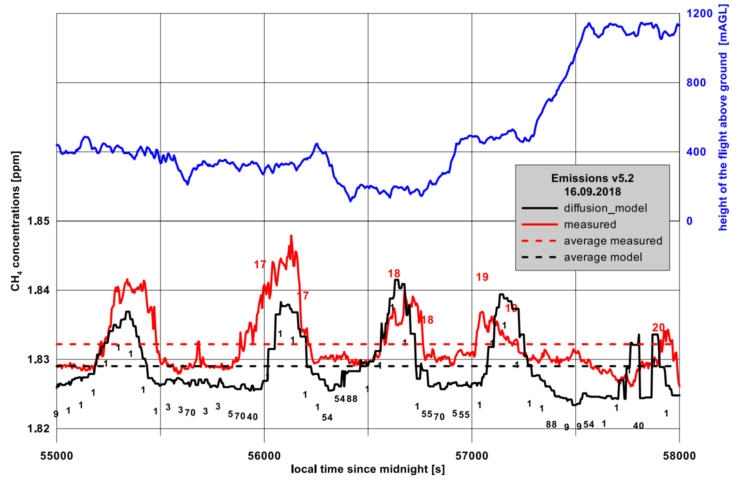

This is the result of a preliminary adjustment for a yet unknown source. The measured signal from crossings on different heights is compared with the dispersion model. Differences in amplitude and width can be used to adjust the distance and strength of the source, after careful adjustment of the basic diffusion parameterisation per flight.

The deficit in the average concentrations from the model (black) against the measurement (red) is indicating underestimated diffuse sources.

Black numbers at the bottom are denoting the dominant sources for the enhanced concentrations against background on this altitude on upwind leg. The red numbers on top of the measured concentrations are identifying bag grab sample numbers (begin and end of fillings).

This offers a maximum of information for continued iterations.

EGU2020-10993 slide 11

SF24: An example of a small part of the working graph used for iteratively fitting emissions upwind of a transect. This example is showing a fit for the plume discussed in more detail in section P. The fit in this case is suffering from the fact that MoDiM is mixing a plume from the surface up to the top of the CBL, while the explicit cross section in figure SF17 is showing that the concentration maximum is at 300 mAGL. More explanations are in the box of this figure.

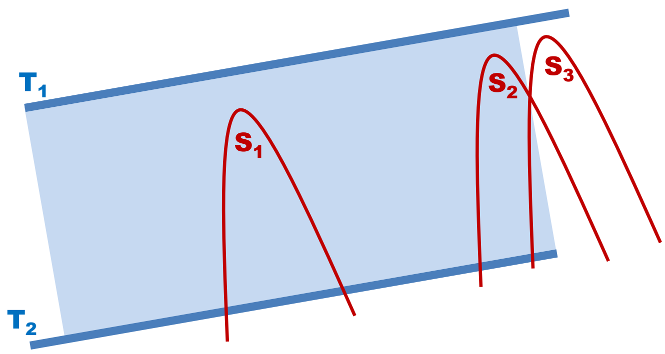

SF25: Three emission sources between the two transects T_1 (upwind) and T_2 (downwind), generating three plumes influencing the concentrations and hence the column masses on the downwind transect T_2. Only S_1 and S_2 are in the area covered by the mass balance (shaded blue), for which the sources from the inventory are counted for a comparison; S_3 is outside. The plume from source S_1 is fully captured in such a mass balance, while the one from S_2 is partly missed and S_3 is adding mass to T_2 from outside the area of the mass balance. A strong source S_2 would lead to an underestimation of the measured balance against the inventory, while a similar source at S_3 would add to the balance but is not counted from the inventory associated with the sub-region.

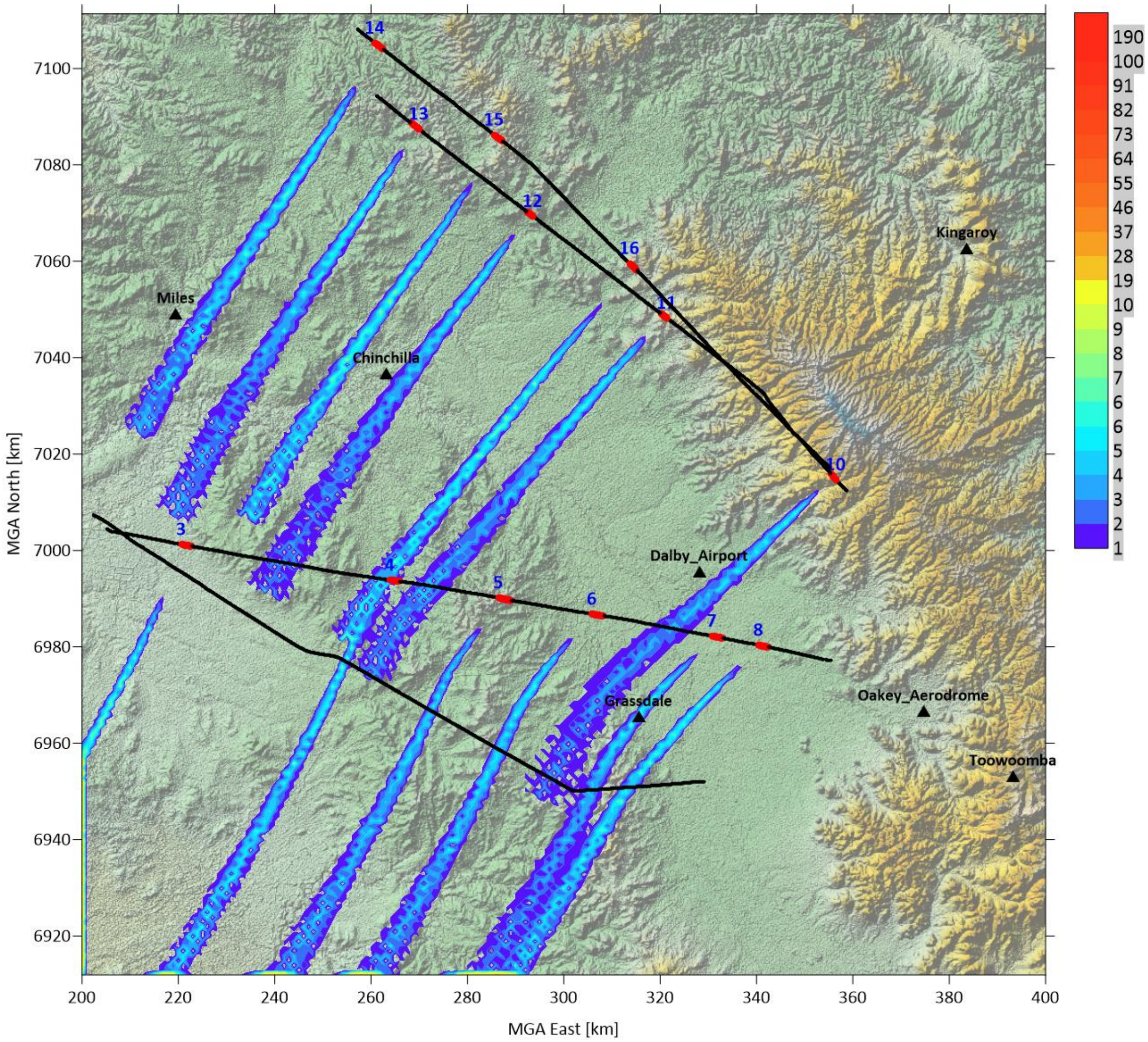

SF26: Backwards trajectories accounting for diffusion (inverse dispersion) starting at positions where bag samples (blue numbers) were taken. These probability densities allowed to estimate where the air in the bag samples was originating from. The colour scale is for the contribution in ppb at the arrival per 1 kg/hr emission at the inverse plume location. This early example was with a relatively narrow widening and did not contain all the features developed later for MoDiM in the forward mode.

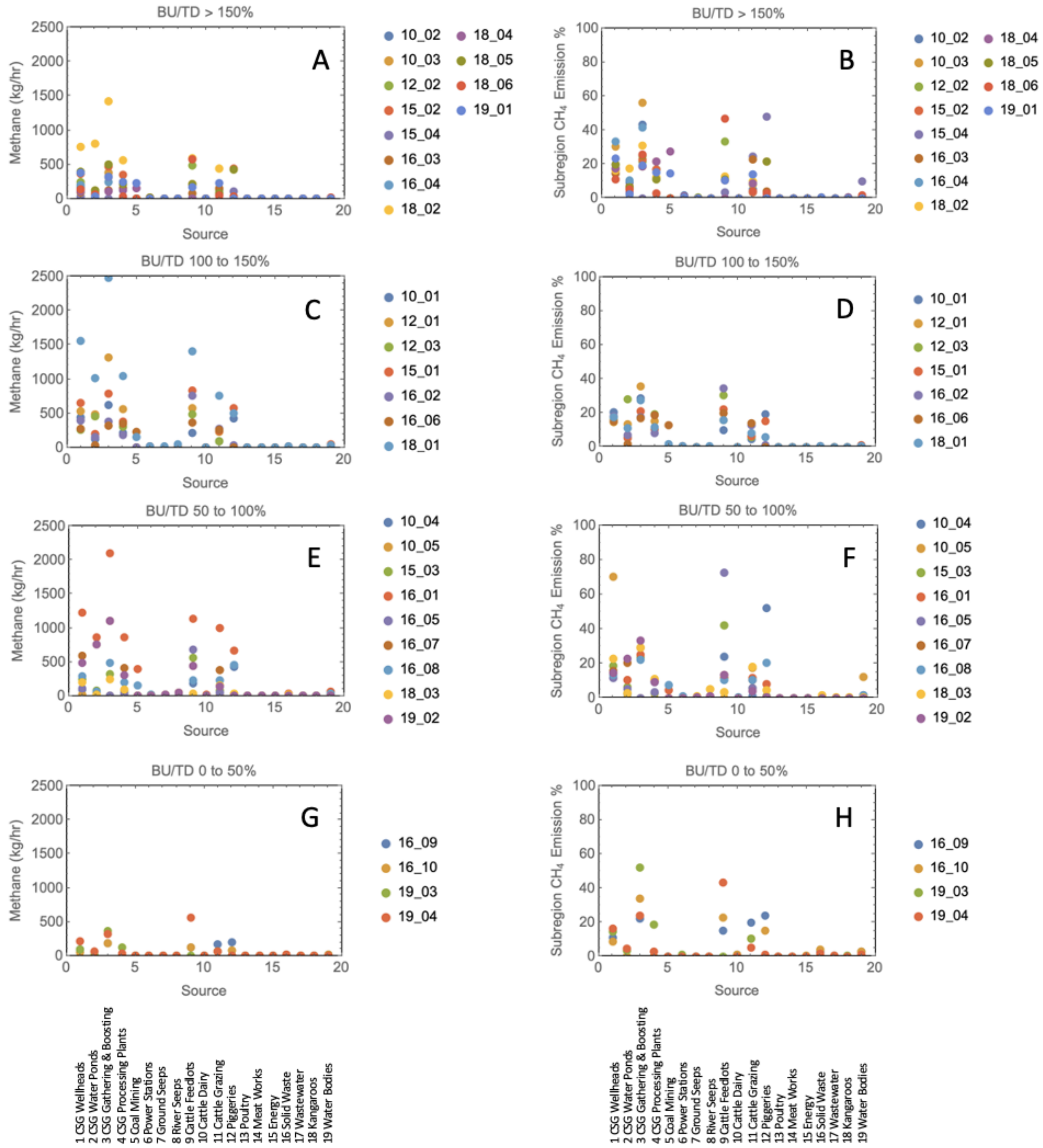

SF27: Methane emissions for each source category within a subregion graphed in clusters of the ratio of the bottom-up/top-down (BU/TD) emission estimates. Each dot refers to an individual sub-region. Plots A, C, E, and G are total BU methane emission rates (kg/hr) vs source categories. Plots B, D, F, and H are the corresponding CH_4 emissions percentages of each BU source category with a subregion vs source categories. The legend corresponds to the subregions in supplementary figures SF7 to SF12.

S Supplementary tables ST1to ST7

Supplementary material for Neininger et al., 2021, Comparing airborne TD emission estimates for methane against BU emission inventories for the Surat Basin, Australia,
Phil. Trans. R. Soc. A. doi: 10.1098/rsta.2020.0458

ST1: UNSW methane emission inventory for the south east portion of the Surat Basin (figures SF1, SF2 and SF3) using data for 2018 (an area of 200 km by 200 km). These estimates were converted to hourly emission rates for comparison with the airborne emission estimate. For comparison, the Katestone inventory, which was used as a prior in [SR10] is provided. The Katestone inventory covers a larger portion of the Surat Basin than this work (350 km by 350 km). See references and notes in table ST2.

Methane Source	Unit	Quantity	Used Emission Factor	UNSW Inventory 2018 (rounded)	Percent of Total Emissions	Katestone Inventory Subset 2015	Katestone Inventory 2015 [SR10]	Note number table ST2
				Methane kg / year	%	Methane kg / year	Methane kg / year	
UNSW Inventory, south east portion of the Surat Basin (figures S1, S2 and S3) Inventory Limits Latitude -28.0 to -26.0, Longitude 149.8 to 151.8						UNSW Inventory Domain	All Surat Basin CSG and western agriculture	
Onshore CSG wells	tonnes of emissions / tonnes of gas throughput	17,027,840	0.000047	800,000	0.44			1a
Abandoned gas onshore wells				57,500	0.03			1b
Venting	Tonnes of emission / tonne of gas flared 28% - Vented (Mm3)	12,799	1.0	13,000,000	7.10			1c
Flaring	Tonnes of emission / tonne of gas flared 72% - Flared (Mm3)	32,912	0.00476	160,000	0.09			1d
CSG Gathering & Boosting Pipelines	tonnes of emissions / pipeline kilometre	4,500	0.23	1,000,000	0.55			1e
Natural Gas Transmission and Storage	tonnes of emissions / pipeline kilometre	2000	0.41	820,000	0.45			1f
CSG Produced Water	Mega litres (ML)	28,823	0.31	8,900,000	4.86			2
CSG Gathering and Boosting Stations	tonnes of emissions / tonnes of gas throughput	14,585,600	0.0015	22,000,000	12.02			3
CSG Processing Plants	tonnes of emissions / tonnes of gas throughput	Various	Mitchell et al. (2015) Gas Processing (1.B.2.b.3) $y = 0.6369\ x^{-0.48}$	9,100,000	4.97			4
Total CSG Estimate				**55,837,500**	**30.51**	**11,556,123**	**16,528,838**	TCSG
Coal Mining	Tonnes of Produced Coal	17,483,772	0.8	14,000,000	7.65	14,418,726	14,424,564	5
Power Stations	N/A	N/A	N/A	280,000	0.15	634,094	640,070	6
Ground Seeps	N/A	N/A	N/A	130,000	0.07	127,714	127,714	7
Condamine River Seeps	N/A	N/A	N/A	380,000	0.21	375,909	375,909	8
Feedlot Cattle	Cattle Population	503,812	70.40	35,000,000	19.12	33,810,847	42,270,444	9
Dairy Cattle	Cattle Population	21,420	110.00	2,400,000	1.31	No estimate	No estimate	10
Grazing (pasture) cattle	Cattle Population	1,014,967	53.89	54,700,000	29.89	25,961,162	92,991,979	11
Total Cattle Estimate				**92,100,000**	**50.32**	**59,772,009**	**135,262,423**	TC
Piggeries	Pig Population	642,261	24.84	16,000,000	8.74	2,037,826	2,358,892	12
Poultry	Bird Population	3,092,051	0.07	220,000	0.12	66,365	96,699	13
Meat Works	kg per processed animal	1,209,610	1.142857143	1,400,000	0.76	No estimate	No estimate	14
Energy 1.A.3.b Road Transportation	Urban Population	57427	Population percentage of Queensland emissions	22,000	0.01	16,138	24,071	15a
Energy 1.A.4.b Residential	Urban Population	57427	Population percentage of Queensland emissions	33,000	0.02	191,525	280,324	15b
Waste 5.A Solid Waste Disposal	Urban Population	57427	Population percentage of Queensland emissions	830,000	0.45	1,409,685	1,905,644	16
Waste 5.D.1 Domestic Wastewater	Urban Population	57427	Population percentage of Queensland emissions	130,000	0.07	816,344	1,137,905	17
Forest nodes - Kangaroos	Kangaroo Population	487,000	0.75	370,000	0.20	No estimate	No estimate	18
On-Farm Water Bodies (Dams)	Hectares	2,319	581	1,300,000	0.71	No estimate	No estimate	19
Total				**183,032,500**	**100**	**91,422,458**	**173,163,053**	
Total Excluding CSG				**127,195,000**		**79,866,335**	**156,634,215**	
Total Coal Seam Gas				**55,837,500**		**11,556,123**	**16,528,838**	

ST2: Notes for Table ST1.

Note Number	Methane Source	Australia. 2020 National Inventory Report https://unfccc.int/documents/228017 Australian Government, National Greenhouse Gas Inventory Report (2020), for inventory year 2018 National Inventory Report 2018, Volume 1. Table, Emission Factors and Data Source (https://www.industry.gov.au/data-and-publications/national-greenhouse-gas-inventory-report-2018)
1a	Onshore CSG wells	• Table 3.44 Fugitive emission factors for natural gas rates determined by [SR7]. • Total gas produced (Mm3), Queensland Government, Queensland-petroleum-production-statistics_2015_2019, Period ending 31/12/2018, doubled for annual estimate https://www.data.qld.gov.au/dataset/petroleum-gas-production-and-reserve-statistics
1b	Abandoned gas onshore wells	• 50% of Queensland inventory estimate for methane emissions for abandoned gas onshore wells https://ageis.climatechange.gov.au
1c	Venting	• Table 3.48 Venting factors. 28% of the Queensland Government Reported Vented and Flaring 67.38 (Mm3)
1d	Flaring	• Table 3.48 Flaring emission factors. 72% of the Queensland Government Reported Vented and Flaring 67.38 (Mm3)
1e	CSG Gathering & Boosting Pipelines	• Table 3.44 Fugitive emission factors for natural gas NGER Method 2 (API 2009) [SR8]. • Google Earth image CSG network length.
1f	Natural Gas Transmission & Storage	• Table 3.44 Fugitive emission factors for natural gas (NGER Method) • Queensland Government Data Portal km of high-pressure pipelines https://www.data.qld.gov.au/dataset/queensland-mining-and-exploration-tenure-series/resource/45b74c74-d725-43ce-9719-e440664c2b95
2	CSG Produced Water	• Table 3.44 Fugitive emission factors for natural gas, NGER Method 2 API 2009 [SR8]. • Produced water volume (ML), Queensland Government, Queensland-petroleum-production-statistics_2015_2019. Six-month period ending 31/12/2018, doubled for annual estimate https://www.data.qld.gov.au/dataset/petroleum-gas-production-and-reserve-statistics
3	CSG Gathering and Boosting Stations	• Table 3.44 Fugitive emission factors for natural gas, [SR9] • Total gas produced (Mm3), Queensland Government, Queensland-petroleum-production-statistics_2015_2019. Period ending 31/12/2018, doubled for annual estimate. https://www.data.qld.gov.au/dataset/petroleum-gas-production-and-reserve-statistics
4	CSG Processing Plants	• Table 3.44 Fugitive emission factors for natural gas. • AEMO Access Market Portals. Actual Flows exported csv file. Data for 16 Sep 2018 used. https://aemo.com.au/energy-systems/gas/gas-bulletin-board-gbb/interactive-map-gbb
TCSG	Total Coal Seam Gas	Sum of categories 1a to 1f, 2, 3 and 4. The Katestone [SR10] combined “Processing and Production” emission estimates is also listed.
5	Coal Mining	• Queensland open cut coal mine emission factor 0.8 kg/tonne • 2017/18 Coal production. https://www.data.qld.gov.au/dataset/coal-industry-review-statistical-tables
6	Power Stations	• New energy production data published 25 March 2020: “Electricity sector emissions and generation data 2018–19” http://www.cleanenergyregulator.gov.au/NGER/National%20greenhouse%20and%20energy%20reporting%20data/electricity-sector-emissions-and-generation-data/electricity-sector-emissions-and-generation-data-2018-19 • Note: There was a large drop in production from the two Braemar power stations.
7	Ground Seeps	• Value reported in [SR10]
8	Condamine River Seeps	• Value reported in [SR10]
9	Cattle Feedlot	• Table 5.12 Implied EFs – Enteric fermentation (CH_4 kg /head/year). Beef Cattle - Feedlot = 67 • Table 5.17 Implied EFs – Manure management (CH_4 kg /head/year) Beef Cattle - Feedlot = 3.4, • Location Data (LD) – A combination of Queensland Government Data Portal (https://www.data.qld.gov.au/dataset/agricultural-land-audit-queensland-series) and “The Farms Transparency Map” (https://map.farmtransparency.org). • Population Count (PC) - Australian Bureau of Statistics 71210DO002_201819 Agricultural Commodities, Australia-2018-19 (https://www.abs.gov.au/statistics/industry/agriculture/agricultural-commodities-australia/latest-release)
10	Dairy Cattle	• Table 5.12 Implied EFs – Enteric fermentation (CH_4 kg /head/year). Dairy Cattle = 95 National Inventory Report 2018, Volume 1, Table 5.17 Implied EFs – Manure management (CH_4 kg /head/year). Dairy Cattle = 15 • LD and PC
11	Cattle Grazing (Pasture)	• Table 5.12 Implied EFs – Enteric Fermentation (CH_4 kg /head/year). Pasture = 51 • Table 5.17 Implied EFs – Manure management (CH_4 kg /head/year). Pasture = 2.89 • LD and PC • Note: For the Condamine statistical area (11a Supplementary Figure S22) the exact head count was used. The emission rate per unit pasture area determined for the Condamine region was applied to pasture areas in the Burnett Mary (11b) and Queensland Murray Darling Basin (11c) Natural Resource Management regions.
TC	Total Cattle	• Sum of all methane emissions from cattle
12	Piggeries	• Table 5.12 Implied EFs – Enteric fermentation (CH_4 kg /head/year) Swine = 1.6 • Table 5.17 Implied EFs – Manure management (CH_4 kg /head/year). Swine = 23.24 • LD and PC
13	Poultry	• Table 5.17 Implied EFs – Manure management (CH_4 kg /head/year). Poultry = 0.07 • LD and PC

14	Meat Works	• AGEIS. https://ageis.climatechange.gov.au https://www.industry.gov.au/data-and-publications/national-greenhouse-gas-inventory-report-2018
15a	Energy 1.A.3.b Road Transportation	• 1,920,000 kg - Queensland methane emissions 2018, Source AGEIS. https://ageis.climatechange.gov.au • Australian Bureau of Statistics 2016 census converted to 2018 estimate, Queensland population 4,990,700
15b	Energy 1.A.4.b Residential	• 2,870,000 kg - Queensland methane emissions 2018, Source AGEIS. https://ageis.climatechange.gov.au • Australian Bureau of Statistics 2016 census converted to 2018 estimate, Queensland population 4,990,700
16	Waste 5.A Solid Waste Disposal	• 72,410,000 kg - Queensland landfill methane emissions 2018. Source AGEIS. https://ageis.climatechange.gov.au • Australian Bureau of Statistics 2016 census converted to 2018 estimate, Queensland population 4,990,700
17	Waste 5.D.1 Domestic Wastewater	• 10,990,000 kg - Queensland wastewater methane emissions 2018, Source AGEIS. https://ageis.climatechange.gov.au • Australian Bureau of Statistics 2016 census converted to 2018 estimate, Queensland population 4,990,700
18	Kangaroos (Forest nodes)	• 487 Forest cells; 40 kangaroos per km^2 Central East, Figure 9, Page 9 (2019 Quota Submissions for Commercially Harvested Macropods in Queensland), https://www.qld.gov.au/__data/assets/pdf_file/0033/88719/quota-submission2019.pdf • 0.75 CH_4 kg per year per kangaroo - [SR11]
19	On-Farm Water Bodies (Dams)	• Queensland Data Portal: (https://www.data.qld.gov.au/dataset/agricultural-land-audit-queensland-series) • Applied to 240 grid cells; 0.61834094 kg/hour per node

Supplementary material for Neininger et al., 2021, Comparing airborne TD emission estimates for methane against BU emission inventories for the Surat Basin, Australia,
Phil. Trans. R. Soc. A. doi: 10.1098/rsta.2020.0458

ST3: Petroleum exploration and production permit numbers for the area studied, and subset of the Queensland Government petroleum gas production and reserve statistics for the period 30/06/2018 to 31/12/2018 (https://www.data.qld.gov.au/dataset/petroleum-gas-production-and-reserve-statistics).

Authorised Holder	**Permit Number**	**Reservoir**	**Field**	**Total Gas produced (Mm³)**	**Flared or Vented (Mm³)**	**Used in Production (Mm³)**	**Water (ML)**	**Wells**
ARROW (DAANDINE) PTY LTD	PL 230	Walloon Coal Measures	Daandine	284.73	1.18	18.03	445.1	135
ARROW (TIPTON) PTY LTD	PL 198	Walloon Coal Measures	Tipton West	163.59	0.77	13.38	444.3	124
ARROW (TIPTON) PTY LTD	PL 238	Walloon Coal Measures	Plainview	2.77	0.01	0.23	14.5	2
ARROW (TIPTON) PTY LTD	PL 260	Walloon Coal Measures	Longswamp	3.19	0.02	0.26	48.1	2
ARROW ENERGY PTY LTD	PL 252	Walloon Coal Measures	Stratheden	53.66	0.17	3.39	386.6	29
AUSTRALIA PACIFIC LNG (CSG) PTY LIMITED	PL 1018	Walloon Coal Measures	Riley	6.05	0.03	0.00	10.8	7
AUSTRALIA PACIFIC LNG PTY LIMITED	PL 1011	Walloon Coal Measures	Alfredson	86.02	0.37	0.00	278.7	33
AUSTRALIA PACIFIC LNG PTY LIMITED	PL 215	Walloon Coal Measures	Orana	611.65	1.99	0.00	1144.3	126
AUSTRALIA PACIFIC LNG PTY LIMITED	PL 226	Walloon Coal Measures	Talinga/Orana	974.11	6.83	1.56	1894.8	212
AUSTRALIA PACIFIC LNG PTY LIMITED	*PL 265*	*Walloon Coal Measures*	*Condabri*	*513.57*	2.18	0.00	550.5	221
AUSTRALIA PACIFIC LNG PTY LIMITED	PL 266	Walloon Coal Measures	Condabri South	552.20	2.34	0.00	482.5	134
AUSTRALIA PACIFIC LNG PTY LIMITED	PL 267	Walloon Coal Measures	Condabri North	503.17	2.14	0.00	587.2	188
AUSTRALIA PACIFIC LNG PTY LIMITED	PL 272	Walloon Coal Measures	Talinga/Orana North	215.61	0.70	0.00	1677.4	78
AUSTRALIAN CBM PTY LTD	PL 194	Walloon Coal Measures	Kogan North	51.59	0.15	4.32	84.2	66
QGC PTY LIMITED	PL 179	Walloon Coal Measures	Argyle	122.69	0.21	7.29	269.0	32
QGC PTY LIMITED	PL 180	Walloon Coal Measures	Codie, Lauren, Kenya	715.47	1.04	19.76	413.4	163
QGC PTY LIMITED	PL 201	Walloon Coal Measures	Berwyndale, Berwyndale South	160.59	0.19	7.83	125.4	78
QGC PTY LIMITED	PL 211	Walloon Coal Measures	Berwyndale	104.83	0.12	5.27	122.6	37
QGC PTY LIMITED	PL 212	Walloon Coal Measures	Berwyndale South	64.75	0.08	3.15	48.3	20
QGC PTY LIMITED	PL 228	Walloon Coal Measures	Kenya, Codie, Kate	402.88	1.53	14.09	753.9	103
QGC PTY LIMITED	PL 229	Walloon Coal Measures	Argyle	99.91	0.16	5.92	235.3	29
QGC PTY LIMITED	PL 247	Walloon Coal Measures	Bellevue	134.11	0.11	4.49	134.6	52
QGC PTY LIMITED	PL 257	Walloon Coal Measures	Jammat	0.19	0.00	0.00	3.2	2
QGC PTY LIMITED	PL 263	Walloon Coal Measures	Matilda-John, Lauren	522.55	0.42	5.18	241.3	100
QGC PTY LIMITED	PL 273	Walloon Coal Measures	Sean, David, Poppy	205.65	0.49	2.02	297.1	116
QGC PTY LIMITED	PL 274	Walloon Coal Measures	Glendower, Harry	12.21	0.02	0.06	5.2	8
QGC PTY LIMITED	PL 275	Walloon Coal Measures	Jen, Ruby Jo, Isabella	931.19	1.36	5.84	715.7	241
QGC PTY LIMITED	PL 276	Walloon Coal Measures	Woleebee Creek, Ross, Kathleen, Cam, Mamdal	1065.56	0.62	7.98	618.6	330
QGC PTY LIMITED	PL 277	Walloon Coal Measures	Kathleen, Cam, Mamdal, Woleebee Creek	434.62	0.24	3.64	283.9	132
QGC PTY LIMITED	PL 278	Walloon Coal Measures	Kenya East, Jammat, Margaret	382.96	4.16	1.77	281.2	109
QGC PTY LIMITED	PL 279	Walloon Coal Measures	Broadwater, Harry, Glendower	865.05	1.26	5.13	543.9	272
QGC PTY LIMITED	PL 442	Walloon Coal Measures	Jordan, Celeste	17.67	0.53	0.33	73.4	28
QGC PTY LIMITED	PL 466	Walloon Coal Measures	Clunie, Barney	24.94	0.03	0.09	12.6	8
QGC PTY LTD	PL 1025	Walloon Coal Measures	Anya	22.10	0.03	1.04	106.6	25
QGC UPSTREAM HOLDINGS PTY LTD	PL 443	Walloon Coal Measures	Owen	77.97	1.23	0.61	77.4	22
QGC UPSTREAM HOLDINGS PTY LTD	PL 458	Walloon Coal Measures	McNulty	279.20	0.65	4.11	606.2	89
QGC UPSTREAM HOLDINGS PTY LTD	PL 459	Walloon Coal Measures	McNulty	10.82	0.03	0.16	109.2	8
QGC UPSTREAM HOLDINGS PTY LTD	PL 472	Walloon Coal Measures	Avon Downs, McNulty	70.26	0.32	2.06	284.6	43
Authorised Holder	**Permit Number**	**Reservoir**	**Field**	**Total Gas produced (Mm³)**	**Flared or Vented (Mm³)**	**Used in Production (Mm³)**	**Water (ML)**	**Wells**
			30/06/2018 to 31/12/2018	**10750.07**	**33.69**	**149.01**	**14411.8**	**3404.00**
			Doubled for an annual rate estimate	**21500.14**	**67.38**	**298.01**	**28823.3**	

Supplementary material for Neininger et al., 2021, Comparing airborne TD emission estimates for methane against BU emission inventories for the Surat Basin, Australia,
Phil. Trans. R. Soc. A. doi: 10.1098/rsta.2020.0458

ST4: Top-down (TD) emission estimates in comparison with the UNSW and Katestone inventories for the same sub-regions bal_10_1 to bal_19_4 (32 cases). The geographical position of the sub-regions is shown in figures SF7 to SF12. **area**: the area of the sub-region; **TD_ref**: The standard TD mass balance calculation for the sub-region (sensitivity cases see ST5): best estimate for the CBL growth, CBL top is defined as m AMSL (section I), wind averaged for those two cases with weak wind (section K); **TD_ref/area**: The emission rate per square kilometre in this sub-region; **BU_1/area**: The UNSW emission estimate per square kilometre; **BU_2/area**: The Katestone emission estimate per square kilometre; **BU_1**: The UNSW emission estimate; **CSG_1**: The emission rate from UNSW CSG sources (type 1 to 4 according to ST1); **rCSG_1**: The percentage of CSG sources in the total UNSW emission estimate; **BU_2**: The Katestone emission estimate; **CSG_2**: The emission rate from CSG sources in the Katestone inventory; **rCSG_2**: The percentage of Katestone CSG sources from the total emissions;

							UNSW (BU_1)				Katestone (BU_2)			
case	balance	area	TD_ref	TD_ref/area	BU_1/area	BU_2/area	BU_1	CSG_1	rCSG_1	BU_1/TD	BU_2	CSG_2	rCSG_2	BU_2/TD
#	day_nbal	km^2	kg/hr	kg CH_4 hr^{-1} km^{-2}	kg CH_4 hr^{-1} km^{-4}	kg CH_4 hr^{-1} km^{-2}	kg/hr	kg/hr	%	%	kg/hr	kg/hr	%	%
1	bal_10_1	1247	1572	1.261	1.793	0.450	2236	1452	65	142	708	372	53	45
2	bal_10_2	578	197	0.341	2.294	1.873	1326	973	73	673	369	241	65	187
3	bal_10_3	441	117	0.265	1.741	0.530	768	693	90	656	62	27	44	53
4	bal_10_4	201	1144	5.692	4.338	0.329	872	234	27	76	376	125	33	33
5	bal_10_5	202	172	0.851	0.554	0.180	112	80	71	65	31	6	19	18
6	bal_12_1	1162	3437	2.958	3.744	0.407	4351	3428	79	127	1398	636	45	41
7	bal_12_2	614	943	1.536	2.674	0.632	1642	916	56	174	596	183	31	63
8	bal_12_3	510	2280	4.471	5.971	0.266	3045	2349	77	134	607	455	75	27
9	bal_15_1	4671	3083	0.660	0.887	0.492	4141	2035	49	134	1516	444	29	49
10	bal_15_2	1399	1212	0.866	1.537	0.588	2150	1327	62	177	713	362	51	59
11	bal_15_3	1254	1850	1.475	1.155	0.115	1448	747	52	78	213	85	40	12
12	bal_15_4	1443	500	0.347	0.782	0.818	1128	56	5	226	409	1	0	82
13	bal_16_1	10716	12186	1.137	0.826	0.333	8849	5111	58	73	4061	1227	30	33
14	bal_16_2	3071	2560	0.834	0.844	0.283	2593	1389	54	101	725	309	43	28
15	bal_16_3	1223	89	0.073	0.752	5.000	920	574	62	1034	445	224	50	500
16	bal_16_4	918	617	0.672	1.269	0.517	1165	1003	86	189	319	237	74	52
17	bal_16_5	1023	1885	1.843	0.974	0.124	996	207	21	53	233	68	29	12
18	bal_16_6	2030	1954	0.963	1.006	0.555	2042	1058	52	105	1084	190	18	55
19	bal_16_7	3406	4492	1.319	1.211	0.277	4126	3137	76	92	1246	688	55	28
20	bal_16_8	3773	3640	0.965	0.641	0.306	2417	1144	47	66	1113	362	33	31
21	bal_16_9	1846	2448	1.326	0.609	0.404	1124	359	32	46	989	231	23	40
22	bal_16_10	1015	3455	3.404	0.705	0.148	716	278	39	21	511	11	2	15
23	bal_18_1	6967	7104	1.020	1.368	0.436	9532	6145	64	134	3099	1311	42	44
24	bal_18_2	2429	2738	1.127	2.044	0.503	4964	3608	73	181	1376	643	47	50
25	bal_18_3	1506	1787	1.187	1.082	0.384	1630	1275	78	91	686	443	65	38
26	bal_18_4	987	482	0.488	1.149	0.737	1134	389	34	235	355	11	3	74
27	bal_18_5	1242	1781	1.434	1.799	0.404	2234	1428	64	125	719	366	51	40
28	bal_18_6	1095	521	0.476	1.194	0.610	1307	581	44	251	318	76	24	61
29	bal_19_1	1260	1135	0.901	1.905	1.130	2400	1629	68	211	1283	401	31	113
30	bal_19_2	1253	3929	3.136	1.601	0.238	2006	1431	71	51	934	678	73	24
31	bal_19_3	822	4475	5.444	0.964	0.116	792	681	86	18	521	228	44	12
32	bal_19_4	1050	3631	3.458	0.742	0.096	779	469	60	21	347	87	25	10
sums and avgs.		61354	77416	1.262	1.222	0.446	74945	46186	62	97	27362	10728	39	35

ST5: Sensitivity cases for the 32 mass balances and two versions of BU estimates associated with the sub-regions. Case, balance, balance and TD_ref see ST4. **TD_m**: TD calculated with the minimum assumption for the CBL growth (section I); **TD_x**: TD calculated with the maximum assumption for the CBL growth; **TD_G**: terrain following CBL (SF20); **TD_Gx**: terrain following CBL and maximum assumption; **TD_Bi**: those cases where the wind was averaged now without averaging and vice-versa; **TD_min**: the minimum solution from all the sensitivity cases; **TD_med**: the median of all the sensitivity cases; **TD_ave**: the average of all the sensitivity cases; **TD_max**: the maximum of all the sensitivity cases; **relerr**: the relative error (± around the median); **err/area**: the error in kg/hr per area (to compare with the average of 1.262 $kg \cdot hr^{-1} \cdot km^{-2}$ of *TD_ref/area* in ST4); **BU_1**: the same as in ST4: the sources of the UNSW inventory picked out within the sub-region and up to 2.5 km outside (for the direct comparison with the Katestone inventory that has a resolution of 5 km only); **BU_1k**: only the sources exactly within the sub-region (1-km-grid), which is not an option for the Katestone inventory.

case	balance	area	TD_ref	TD_m	TD_x	TD_G	TD_Gx	TD_Bi	TD min	TD med	TD ave	TD max	relerr	err/area	BU_1	BU_1k
#	day_nbal	km^2	kg/hr	kg/hr	kg/hr	kg/hr	kg/hr	kg/hr	kg/hr	kg/hr	kg/hr	kg/hr	%	$kg\ CH_4\ hr^{-1}\ km^{-1}$	kg/hr	kg/hr
1	bal_10_1	1247	1572	1430	1699	1516	1643	1392	1392	1544	1542	1699	10%	0.12	2236	2190
2	bal_10_2	578	197	134	214	159	209	142	134	178	176	214	22%	0.07	1326	876
3	bal_10_3	441	117	64	144	94	129	87	64	106	106	144	38%	0.09	768	670
4	bal_10_4	201	1144	1110	1209	1144	1179	879	879	1144	1111	1209	14%	0.82	872	813
5	bal_10_5	202	172	167	204	172	190	155	155	172	177	204	14%	0.12	112	37
6	bal_12_1	1162	3437	3210	3500	3477	3547	2904	2904	3457	3346	3547	9%	0.28	4351	3716
7	bal_12_2	614	943	863	892	925	879	1003	863	909	918	1003	8%	0.11	1642	1478
8	bal_12_3	510	2280	2186	2365	2350	2396	1710	1710	2315	2215	2396	15%	0.67	3045	2158
9	bal_15_1	4671	3083	2809	3576	3139	3674	2999	2809	3111	3213	3674	14%	0.09	4141	3775
10	bal_15_2	1399	1212	1255	1297	1216	1358	806	806	1236	1191	1358	22%	0.20	2150	2057
11	bal_15_3	1254	1850	1771	2153	1907	2191	1681	1681	1879	1926	2191	14%	0.20	1448	1354
12	bal_15_4	1443	500	336	613	500	626	738	336	557	552	738	36%	0.14	1128	242
13	bal_16_1	10716	12186	9038	13696	13146	14879	10278	9038	12666	12204	14879	23%	0.27	8849	8485
14	bal_16_2	3071	2560	524	2768	2600	2743	2772	524	2672	2328	2772	42%	0.37	2593	2196
15	bal_16_3	1223	89	-1076	-7	282	118	77	-1076	83	-86	282	818%	0.56	920	685
16	bal_16_4	918	617	98	727	501	611	575	98	593	522	727	53%	0.34	1165	603
17	bal_16_5	1023	1885	1497	2092	1842	2049	2150	1497	1967	1919	2150	17%	0.32	996	942
18	bal_16_6	2030	1954	1318	2123	2035	2293	334	334	1995	1676	2293	49%	0.48	2042	1838
19	bal_16_7	3406	4492	3339	4977	4765	5360	4107	3339	4629	4507	5360	22%	0.30	4126	3806
20	bal_16_8	3773	3640	2667	4217	3801	4432	3647	2667	3724	3734	4432	24%	0.23	2417	2210
21	bal_16_9	1846	2448	1962	2771	2915	3218	2531	1962	2651	2641	3218	24%	0.34	1124	851
22	bal_16_10	1015	3455	2784	3998	3748	4251	4027	2784	3873	3711	4251	19%	0.72	716	554
23	bal_18_1	6967	7104	6509	7772	7234	7953	7773	6509	7503	7391	7953	10%	0.10	9532	9090
24	bal_18_2	2429	2738	2625	2933	2737	2962	2867	2625	2803	2810	2962	6%	0.07	4964	4590
25	bal_18_3	1506	1787	1653	1952	1837	1995	2203	1653	1895	1905	2203	15%	0.18	1630	871
26	bal_18_4	987	482	406	555	507	579	457	406	495	498	579	17%	0.09	1134	600
27	bal_18_5	1242	1781	1630	1936	1846	2001	1986	1630	1891	1863	2001	10%	0.15	2234	2019
28	bal_18_6	1095	521	381	623	520	651	470	381	521	528	651	26%	0.12	1307	1228
29	bal_19_1	1260	1135	1150	1135	1113	1112	785	785	1124	1072	1150	16%	0.14	2400	1614
30	bal_19_2	1253	3929	3844	3903	4000	4008	3828	3828	3916	3919	4008	2%	0.07	2006	3328
31	bal_19_3	822	4475	4193	4319	4680	4499	4830	4193	4487	4499	4830	7%	0.39	792	699
32	bal_19_4	1050	3631	3389	4197	3819	4330	2751	2751	3725	3686	4330	21%	0.75	779	1307
sums and avgs.		61354	77416	63266	84553	80527	88065	72944	63266	78972	77795	88065	16%	0.20	74945	66882

ST6: Aggregated emission estimates for the full TD domain (reference cases and sensitivity cases); details in section G. **TD**: top-down emission estimates based on the mass balances; **BU**: bottom-up emission estimates from the two emission inventories; **CSG**: CSG-emission estimate within BU; **rCSG**: the ratio of CSG/BU; **BU/TD**: the percentage of TD that is estimated by the inventories; **bal_16_1+bal_16_2**: the sum of the two large sub-regions shown in SF6 and SF10 (reference cases only). The sensitivity cases are the same as in ST5. The minimum, median, average and maximum are characterising the range of aggregated results compared with the UNSW inventory for the same TD domain. **TD_nor** for Katestone is using the same method as for TD_ref for UNSW, however, since the aggregation uses geographical information from the inventory, the results are not the same.

	TD	BU	CSG	rCSG	BU/TD
	kg/hr	kg/hr	kg/hr	%	%
TD vs. Katestone:					
bal_16_1+bal_16_2	**14746**	**4786**	**1536**	**32%**	**32%**
TD_nor	**15269**	**4847**	**1312**	**27%**	**32%**
TD vs. UNSW:					
bal_16_1+bal_16_2	14746	11442	6500	57%	78%
TD_ref	13499	11531	6202	54%	85%
TD_min	10886	11531	6202	54%	106%
TD_max	14786	11531	6202	54%	78%
TD_Gx	15494	11531	6202	54%	74%
TD_Bi	13092	11597	6201	53%	89%
minimum	**10886**	**11442**	**6201**	**54%**	**105%**
median	**13414**	**11531**	**6202**	**54%**	**86%**
average	**13636**	**11536**	**6239**	**54%**	**85%**
maximum	**15494**	**11597**	**6500**	**56%**	**75%**

ST7 is listing the background concentrations and their temporal changes during the six days with mass balance calculations. **time_1** and **time_2** are the times in the first and last phases of the flights where the minima **conc_1** and **conc_2** were found in the lower CBL. **dconc** is the difference, and **dconc/dt** the temporal trend.

date d.m.y	time_1 h LT	time_2 h LT	conc_1 ppm	conc_2 ppm	dconc ppb	dconc/time ppb/hr
10.09.2018	11.34	13.27	1.82508	1.82752	2.433	1.261
12.09.2018	12.62	15.74	1.82297	1.82362	0.650	0.208
15.09.2018	10.98	13.38	1.82672	1.82932	2.600	1.083
16.09.2018	10.04	16.17	1.82200	1.82200	0.000	0.000
18.09.2018	10.24	14.13	1.82282	1.82525	2.433	0.625
19.09.2018	10.68	16.31	1.82427	1.82395	-0.317	-0.056

T Supplementary References SR1 to SR2

SR1. Lu, X., Harris, S. J., Fisher, R. E., Lowry, D., France, J. L., Hacker, J., Neininger, B., Röckmann, T., van der Veen, C., Menoud, M., Schwietzke, S., and Kelly, B. F. J. (2020) Methane Source Attribution Challenges in the Surat Basin, Australia, EGU General Assembly 2020, Online, 4–8 May 2020, EGU2020-12508, https://doi.org/10.5194/egusphere-egu2020-12508 https://presentations.copernicus.org/EGU2020/EGU2020-12508_presentation.pdf

SR2. Lu, X., Harris, S. J., Fisher, R. E., France, J. L., Nisbet, E. G., Lowry, D., Röckmann, T., van der Veen, C., Menoud, M., Schwietzke, S., and Kelly, B. F. J. (2021) Isotopic Signatures of Major Methane Sources in the Coal Seam Gas Fields and Adjacent Agricultural Districts, Queensland, Australia, Atmos. Chem. Phys. Discuss. [preprint], https://doi.org/10.5194/acp-2021-76, in review.

SR3. Blackadar A.K., 1998. Turbulence and Diffusion in the Atmosphere. 185 pp. Springer. ISBN 3-540-61406-0

SR4. Cebeci, T. and J. Cousteix. 1999. Modeling and Computation of Boundary-Layer Flows. Springer. ISBN3-540-65010-5.

SR5. Foken, T., M. Aubinet, J. J. Finnigan, M. Y. Leclerc, M. Mauder, and Kyaw Tha Paw U. 2011. Results of a panel discussion about the energy balance closure correction for trace gases. BAMS ES13, http://dx.doi.org/10.1175/2011BAMS3130.1

SR6. Isaac P.R. 2004. Estimating Surface-Atmosphere Exchange at Regional Scales. PhD Thesis at the School of Chemistry, Physics and Earth Sciences, Faculty of Science and Engineering, The Flinders University of South Australia.

SR7. Day, S., Dell'Amico, M., Fry, R., Javanmard Tousi, H., (2014). Field Measurements of Fugitive Emissions from Equipment and Well Casings in Australian Coal Seam Gas Production Facilities. CSIRO, Australia.

SR8. API (2009) The American Petroleum Institute Compendium of Greenhouse Gas Emissions Estimation Methodologies for the Oil and Natural Gas Industry. (https://www.api.org/~/media/files/ehs/climate-change/2009_ghg_compendium.ashx)

SR9. Mitchell, Austin L. and Tkacik, Daniel S. and Roscioli, Joseph R. and Herndon, Scott C. and Yacovitch, Tara I. and Martinez, David M. and Vaughn, Timothy L. and Williams, Laurie L. and Sullivan, Melissa R. and Floerchinger, Cody and Omara, Mark and Subramanian, R. and Zimmerle, Daniel and Marchese, Anthony J. and Robinson, Allen L. (2015) Measurements of Methane Emissions from Natural Gas Gathering Facilities and Processing Plants: Measurement Results. Env. Sci. & Tech., 49(5), 3219-3227, doi:10.1021/es5052809.

SR10. Luhar, A., D. Etheridge, Z. Loh, J. Noonan, D. Spencer, L. Smith, and C. Ong. 2020. Quantifying Methane Emissions from Queensland's Coal Seam Gas Producing Surat Basin Using Inventory Data and an Efficient Regional Bayesian Inversion. Atmos. Chem. Phys. doi:10.5194/acp-2020-337.

SR11. Vendl, C., Clauss, M., Stewart, M., Legget, K., Hummel, J., Kreuzer, M., Munn, A. (2015) Decreasing methane yield with increasing food intake keeps daily methane emissions constant in two foregut fermenting marsupials, the western grey kangaroo and red kangaroo. J. Exp. Biol., 2015, 218: 3425-3434; doi: 10.1242/jeb.128165